AD-A066 252   CALIFORNIA RESEARCH AND TECHNOLOGY INC WOODLAND HILLS   F/G 11/2
                NUMERICAL INVESTIGATIONS OF FRACTURE AND MICRO-MECHANICS IN CER--ETC(U)
                JAN 79   Y M ITO, M ROSENBLATT, L DEANGELO   N00014-77-C-0790

UNCLASSIFIED   NL

| OF |
ADA
066252

C/R/T

California Research & Technology, Inc.

LEVEL

REPORT N00014-77-C-0790

NUMERICAL INVESTIGATIONS OF FRACTURE AND
MICRO-MECHANICS IN CERAMICS

JANUARY 1979

FINAL REPORT FOR PERIOD 15 SEPTEMBER 1977–14 SEPTEMBER 1978

DDC

MAR 26 1979

A

PREPARED FOR

OFFICE OF NAVAL RESEARCH
800 NORTH QUINCY STREET
ARLINGTON, VIRGINIA 22217
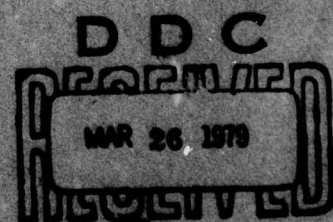
79 01 29 015

DISCLAIMER NOTICE

THIS DOCUMENT IS BEST QUALITY
PRACTICABLE. THE COPY FURNISHED
TO DDC CONTAINED A SIGNIFICANT
NUMBER OF PAGES WHICH DO NOT
REPRODUCE LEGIBLY.

REPORT DOCUMENTATION PAGE		READ INSTRUCTIONS BEFORE COMPLETING FORM
1. REPORT NUMBER N00014-77-C-0790	2. GOVT ACCESSION NO.	3. RECIPIENT'S CATALOG NUMBER
4. TITLE (and Subtitle) Numerical Investigations of Fracture and Micro-Mechanics in Ceramics.		5. TYPE OF REPORT & PERIOD COVERED Final Report 15 Sep 1977 — 14 Sep 1978 6. PERFORMING ORG. REPORT NUMBER
7. AUTHOR(S) Y. Marvin Ito, Martin Rosenblatt, Larry DeAngelo, and Louis Y. Cheng		8. CONTRACT OR GRANT NUMBER(s) N00014-77-C-0790
9. PERFORMING ORGANIZATION NAME AND ADDRESS California Research & Technology, Inc. 6269 Variel Avenue, Suite 200 Woodland Hills, California 91367		10. PROGRAM ELEMENT, PROJECT, TASK AREA & WORK UNIT NUMBERS
11. CONTROLLING OFFICE NAME AND ADDRESS Office of Naval Research 800 North Quincy Street Arlington, Virginia 22217		12. REPORT DATE January 1979 13. NUMBER OF PAGES
14. MONITORING AGENCY NAME & ADDRESS(If different from Controlling Office) 67 p.		15. SECURITY CLASS. (of this report) Unclassified 15a. DECLASSIFICATION/DOWNGRADING SCHEDULE

16. DISTRIBUTION STATEMENT (of this Report)

17. DISTRIBUTION STATEMENT (of the abstract entered in Block 20, if different from Report)

18. SUPPLEMENTARY NOTES

19. KEY WORDS (Continue on reverse side if necessary and identify by block number)

Crack activation; numerical simulation; subsonic water drop impact; surface flaws; surface pore; silicon nitride; second phase particles; inclusion; crack extension; crack arrest; strain energy release.

20. ABSTRACT (Continue on reverse side if necessary and identify by block number)

This document contains three technical papers:
1. "Surface Flaw Effects on Crack Propagation from Subsonic Water Drop Impact"
The effects of surface flaws on ceramic target damage from subsonic water drop impacts are investigated using numerical code simulations based on fundamental wave propagation and fracture mechanics concepts. The water drop impact generates a tensile stress wave with a steep near-surface gradient. As a consequence of this steep stress gradient, crack activation is dependent on the depth of surface flaws. In addition, a relatively large flaw can perturb the stress field such that crack
(Cont'd.)

DD FORM 1473 EDITION OF 1 NOV 65 IS OBSOLETE

20. activation in its vicinity is suppressed.

2. "Effects of Surface Pores in Silicon Nitride Impacted by a Water Drop"
A water drop impacting directly on a surface pore may significantly increase
the probability of crack formation and growth near the pore boundary. To
examine this physical process, the dynamics of a 335 m/s water drop impact on
a silicon nitride target with a 40 micron diameter hemispherical surface pore
has been simulated using a finite difference computer code called WAVE-L.

The maximum tensile stress in the silicon nitride target is about 15 kbar =
1.5 GPa and occurs at the bottom of the hemispherical pore on the axis of
cylindrical symmetry. The tensile stresses at the bottom of the pore have a
duration of about 15 ns.

Microstructural failure of the silicon nitride material near the bottom of the
pore appears likely based on the large predicted tensile stresses and the
large predicted stress intensity factors.

3. "Strain Energy Release Associated with Circumferential Cracks Around
    Embedded Particles"
Numerical code simulations are used to determine the strain energy release
associated with circumferential cracks around spherical particles embedded in
tension within homogeneous matrix materials. It is shown that the fractional
release of strain energy $f(\mu)$, where μ is the normalized crack size and
$f(0)=1$ for no crack and $f(\pi)=0$ for a crack all around the particle, has a
point of inflection at about $\mu=\pi/2$ (hemispherical crack). A *single* point of
inflection in $f(\mu)$ confirms the theoretical conditions of crack extension and
arrest proposed by F. F. Lange in "Criteria for Crack Extension and Arrest
in Residual, Localized Stress Fields Associated with Second Phase Particles"
(Fracture Mechanics of Ceramics, Vol. 2, ed. by Bradt, Hasselman and Lange,
pp. 599-613, Plenum Press, New York, 1974).

SUMMARY

This report contains a collection of technical papers which cover three important areas in the development of physical relationships between microstructure and fracture in ceramics. Each section in this report covers one of the following investigations:

1. Surface flaw effects on crack propagation from subsonic water drop impact.

2. Effects of surface pores in silicon nitride impacted by a water drop.

3. Strain energy release associated with circumferential cracks around embedded particles.

SECTION I

Surface Flaw Effects on Crack Propagation
from Subsonic Water Drop Impact

SURFACE FLAW EFFECTS ON CRACK PROPAGATION FROM SUBSONIC WATER DROP IMPACT[1]

Y. Marvin Ito, Martin Rosenblatt

California Research & Technology, Inc.
Woodland Hills, Ca. 91367

The effects of surface flaws on ceramic target damage from subsonic water drop impacts are investigated using numerical code simulations based on funda- mental wave propagation and fracture mechanics concepts. The water drop impact generates a tensile stress wave with a steep near-surface gradient. As a con- sequence of this steep stress gradient, crack activation is dependent on the depth of surface flaws. In addition, a relatively large flaw can perturb the stress field such that crack activation in its vicinity is suppressed.

Key Words: Crack activation; numerical simulation; subsonic water drop impact; surface flaws.

1. Introduction

The damage of a ceramic target from a subsonic water drop impact is dependent on the tensile stresses generated by the impact and the criteria for the extension of flaws ex- posed to the tensile stress field. Since the target response is essentially elastic, the maximum tensile stresses are the radial stress components. Also, the tensile stress field has a steep near-surface gradient. Thus, these radial stresses tend to produce circumfer- ential cracks which initiate at the surface and propagate into the target [1][2].

As a consequence of the relatively steep near-surface stress gradient, it is expected [1] that crack activation is dependent on the depth of surface flaws (exposed to this stress gradient). It is the intent of this paper to analyze this effect for specified im- pact conditions.

2. Approach

A series of *numerical simulations* are performed in order to examine the effects of surface flaws on *zinc selenide* window damage from subsonic water drop impact. The normal impact conditions of a $2R_0$ diameter water drop onto the window target at velocity V_0 is shown in figure 1. A finite-difference computer code, WAVE-L, with an analytic pressure loading model is used to predict the target response.

WAVE-L is a two-dimensional (axial or plane symmetry), Lagrangian, explicit, finite- difference code based on the HEMP scheme [2] which integrates the governing partial dif- ferential equations of motion for arbitrary dynamic problems in solid and fluid mechanics. It has been applied in a number of particle impact investigations, including both sub- sonic [3] and hypersonic [4] erosion.

The analytic pressure loading model has been developed for simulating subsonic water drop impacts and is discussed elsewhere [5]. The impact model specifies the loading pres- sure on the target surface as a function of radius from the impact point and time, $P(r,t)$.
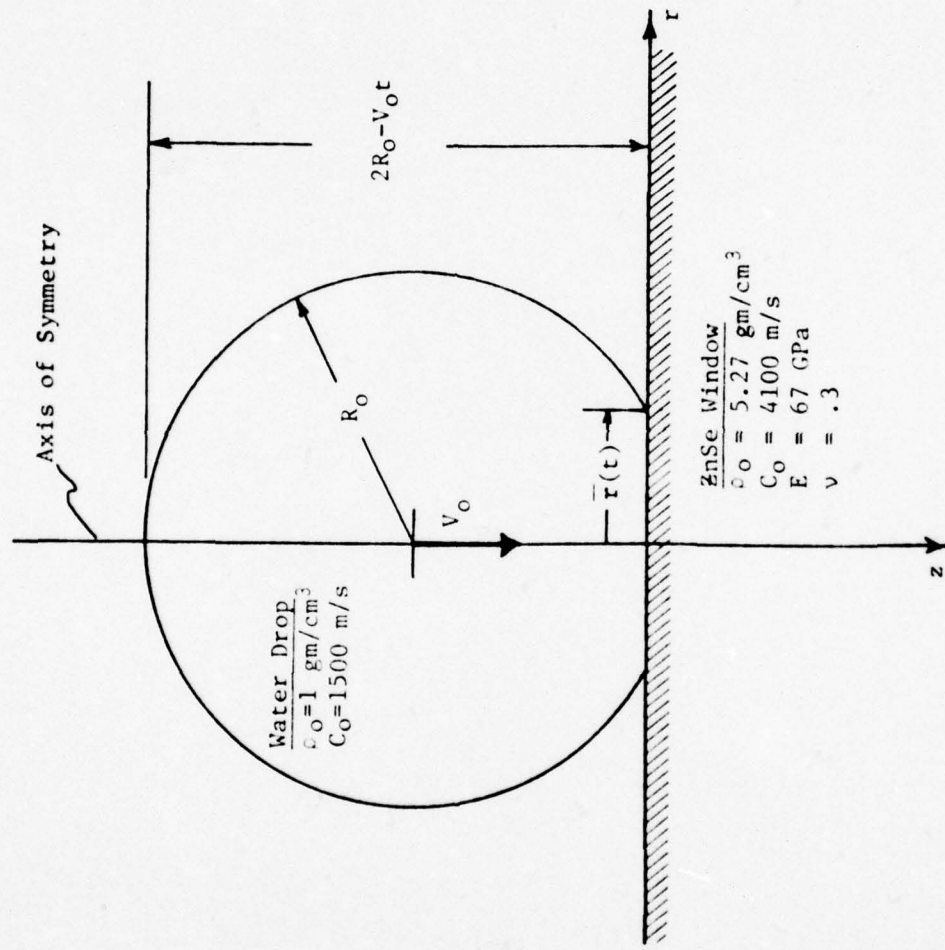
Figure 1. Normal impact conditions of $2R_o$ water drop onto zinc selenide (ZnSe) window at velocity V_o.

The development of this analytic loading model was based on *detailed* WAVE-L numerical calculations [5] of spherical water drop impact onto a rigid surface. The rigid surface approximation is valid when the target surface deflection is negligible compared to the drop radius. For elastic materials, this condition is satisfied if the target material impedance (density times wave speed) is much greater than the water impedance. The zinc selenide targets described in this paper have an impedance which is 14 times greater than water. Hence, the *decoupled* approach is justified in the present case.

The loading pressure function, $P(r,t)$, for a water drop of 2-mm diameter $(2R_O)$ impacting at 222 m/s (730 fps) velocity (V_O) onto a zinc selenide (ZnSe) window target has been determined [5]. Figure 2 gives the maximum impact pressure profile. Due to the spherical geometry and water material properties, an off-axis peak[3] pressure occurs (at early times) which is about twice the Hugoniot value. This peak pressure occurs when the velocity of the radius of contact ($\bar{r}$ in fig. 1) approximately equals the speed of sound (C_O) in water [5].

This impact pressure $P(r,t)$ is used as the loading boundary condition for the axisymmetric WAVE-L numerical calculation of the ZnSe target response. Figure 3 shows the initial computational grid for the target material using 80 cells per water drop diameter $(2R_O = 2mm)$. In the WAVE-L code, particle velocity is defined at the corners of the computational cells while the stress state is associated with the center of the cells.

Figure 4 indicates typical *elastic response* of a ZnSe window in terms of the particle velocity field and principal in-plane (r,z) *tensile* stress field at 0.1 µs. The velocity vectors show the magnitude and direction of the velocity of the particle mass located at the tail of the vector. A 15-m/s (50-fps) scale bar is shown in the upper right corner of the figure. The principal tensile stresses are indicated by lines which show their magnitude and direction in the r-z plane. (Hoop tensile stresses are not indicated on these plots.) A 1-bar (14500-psi) scale bar is shown in the upper left corner of these plots. Thus, at 0.1 µs after the impact, the peak velocities are roughly 15 m/s (50 fps) in the target and the peak tensile stresses are about 2 kbar (30000 psi).

It is seen that a region of high tensile stresses occurs *near* the surface, outside the contact area. The material directly under the contact area is in pure compression. Figure 5 shows the corresponding velocity and in-plane tensile stress fields at 0.2 µs. The qualitative features are similar to the 0.1-µs plot; however, the peak velocities and peak tensile stresses have already decayed below the 0.1-µs values.

The specified impact conditions used in the present numerical simulations involve 222 m/s (730 fps) impact of 2-mm diameter water drop onto zinc selenide windows. These conditions are considered to be representative of subsonic liquid drop impact onto ceramic targets. In the following, Section 3 gives details of the near-surface stress gradient, Section 4 shows the effect of surface flaws and Section 5 has the concluding discussion.

3. Near-Surface Stress Gradient

The formation of high tensile stresses near the surface of a ZnSe target impacted by a water drop is illustrated in figures 4 and 5 (Section 2). In this numerical simulation the initial computational grid (fig. 3 in Section 2) has 40 cells per water drop radius. Since the effective prediction of crack activation requires that these high tensile stresses be well characterized, an appropriate fine-zoned computational grid must be selected. Some calculations, employing selected fine-zoned computational grids in the near-surface impact region, provide a basis for selecting the grid structure for subsequent crack activation experiments.

---

[3]Note that this pressure peak will not occur for subsonic *solid* particle impacts; and observed differences in target response from solid versus liquid projectile impacts may be partially due to the presence of the off-axis pressure peak.
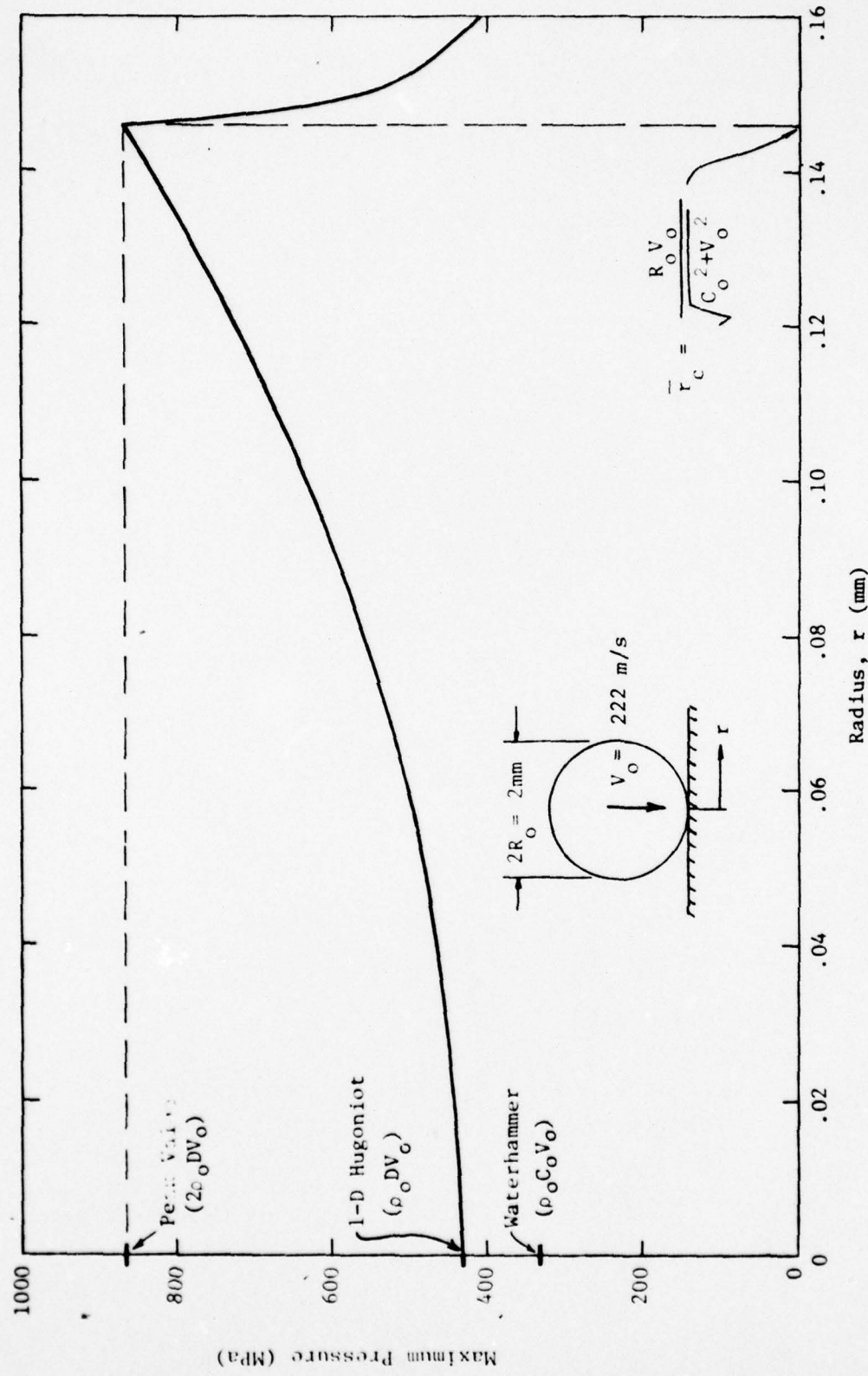
Figure 2. Maximum impact pressure as a function of radial distance from impact center for 222-m/s impact of 2-mm water drop onto ZnSe window.
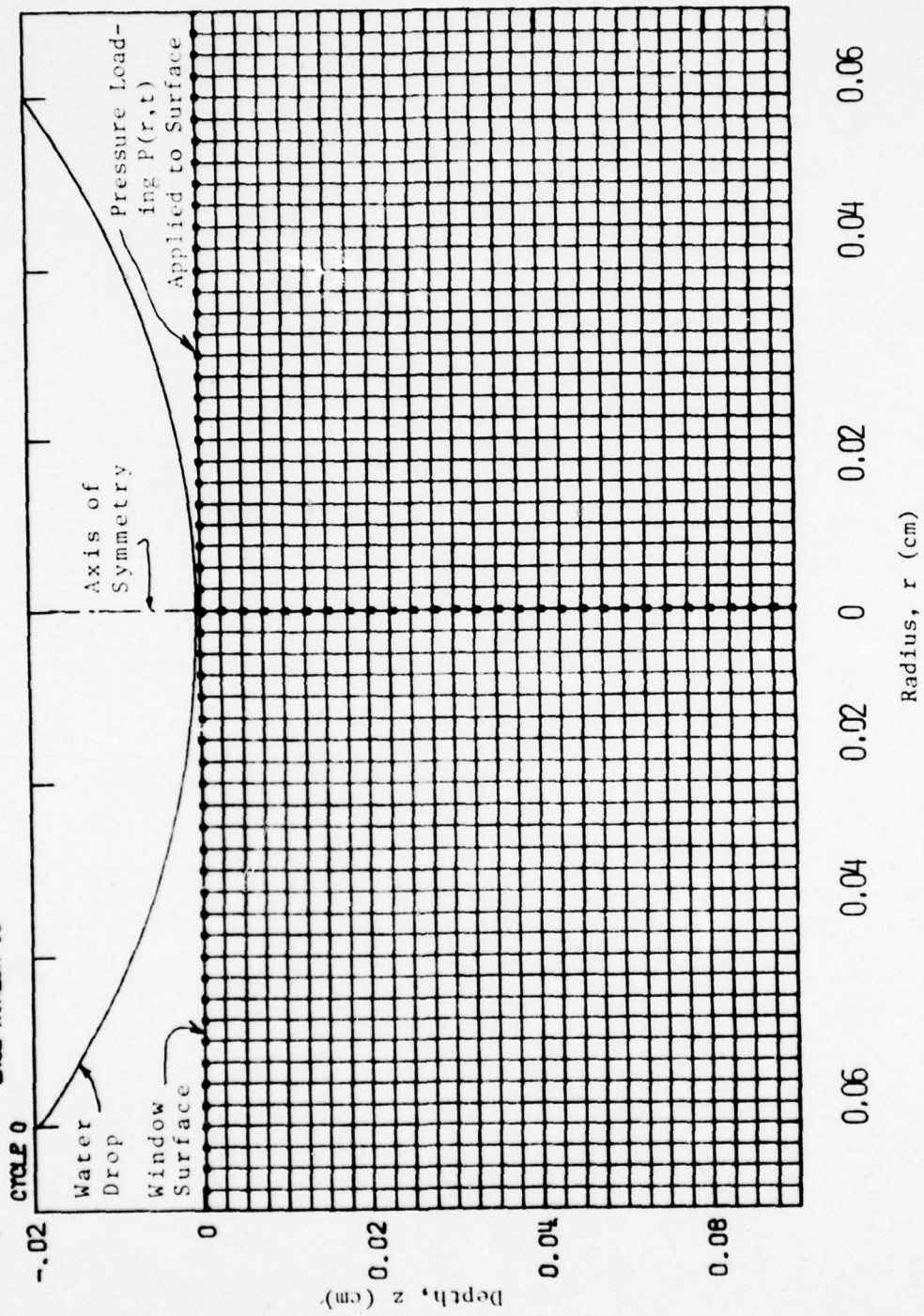
Figure 3. Initial computational grid in target material using 80 cells per 2-mm water drop diameter.
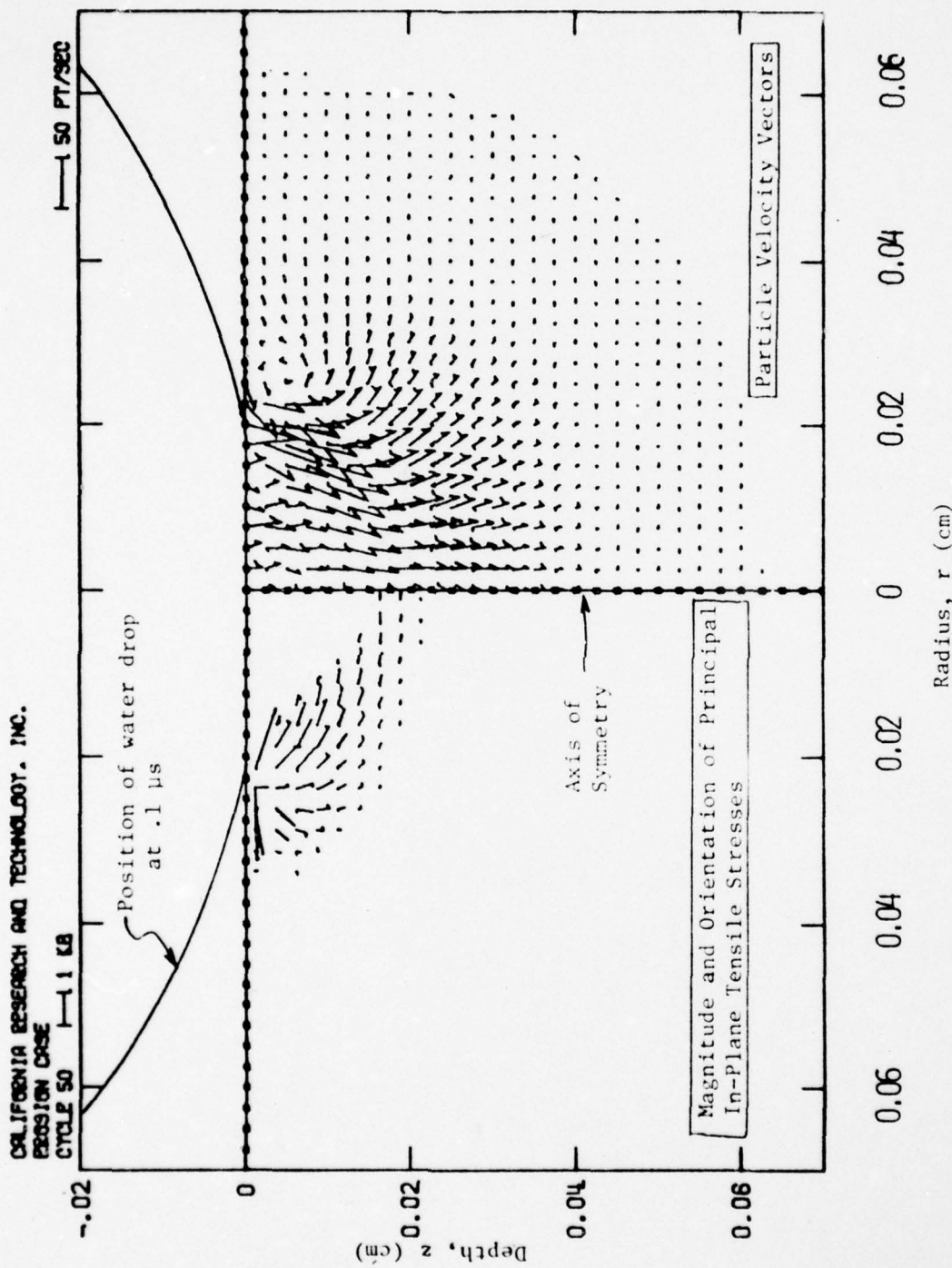
Figure 4. Elastic response of ZnSe window for 222-m/s impact of 2-mm water drop at 0.1 μs (80 computational cells per drop diameter).
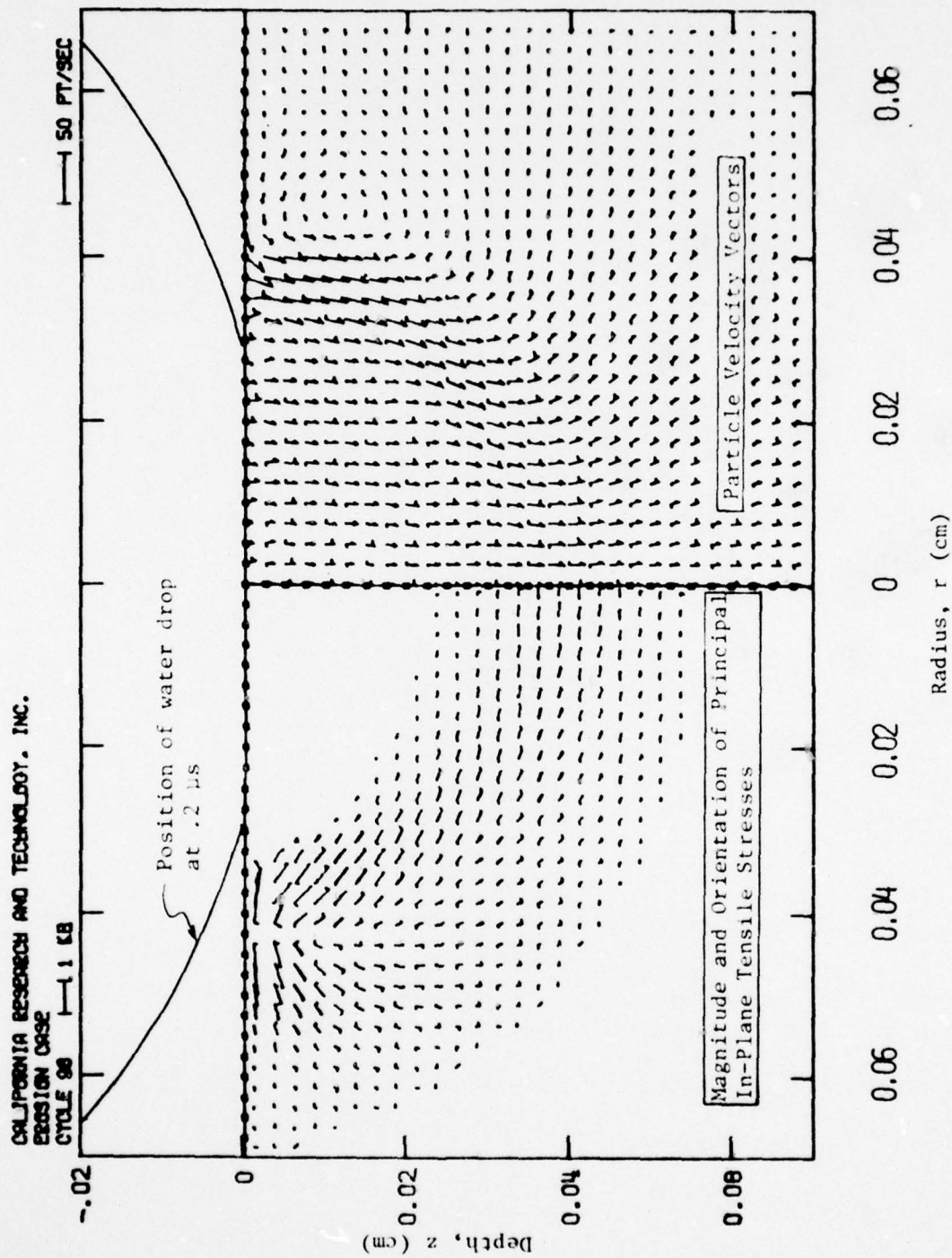
Figure 5. Elastic response of ZnSe window for 222-m/s impact of 2-mm water drop at 0.2 μs (80 computational cells per drop diameter).

Figure 6 shows the peak tensile stress versus depth in a ZnSe window impacted by a water drop at 222 m/s (730 fps) for three variations in computational cell size. Note the very steep stress gradient near the impact surface and its increased resolution[4] with decreased cell size (where stress is defined at the cell center). For a water drop of 1-mm radius[5] the finest-zoned (80 cells per drop radius) case is adequate to resolve peak tensile stress from 356 MPa (52000 psi) at a depth of about 6 μm to 80 MPa (12000 psi) at 100 μm depth.

Figure 7 shows the peak tensile (radial) stress near the surface versus radius. The results are from the surface computational cells which have stress defined at the cell center depth of $z = R_O/160$ or 6.25 μm. The maximum in the peak tension (356 MPa) occurs at radius $r_p \approx 0.2 R_O$ or 200 μm. For $r < 0.1 R_O$ or 100 μm no tension develops in the target surface. At radius $2 r_p \approx 0.4 R_O$ or 400 μm the peak tension has dropped to only 200 MPa (30000 psi). The nominal static tensile strength of ZnSe is about 45 MPa (6500 psi).

The temporal development of the radial tensile stress at four radial locations ($3/4 r_p$, r_p, $3/2 r_p$ and $2 r_p$) near the target surface is given in figure 8. The pulse duration (which is about 30 ns at the maximum tension location r_p) increases with radial location (~60 ns at $3/2 r_p$ and ~75 ns at $2 r_p$).

The effect of a surface flaw of depth $R_O/80$ or 12.5 μm at radius $r_p \approx 0.2 R_O$ or 200 μm on the peak *radial* tensile stress is shown on figure 9. For this flaw, the stress gradient ahead of the crack tip is similar to that from the surface without a flaw, but the maximum in the peak radial tension is about 10 percent less.

It is concluded that the effects of surface flaws of depths from 10 μm and greater, which are exposed to these stress gradients, should be well characterized in subsequent crack activation experiments using the fine-zoned computational grid with 80 cells per drop radius.

4. Surface Flaw Effects

In the numerical code a flaw is simulated as "tensile" cracks across computational cells near the surface. In a cell with an initial crack, no tensile stress across the crack is permitted, and no shear stress is permitted on the crack if the crack is open (the width of the crack is continuously monitored). These stress adjustments are important because a crack frequently alters the local stress field in such a way as to enhance its own growth. Thus, any realistic method of predicting crack growth must consider the altered stress field.

The crack activation experiments involve surface flaws of various depths located at radius $3/2 r_p \approx 0.3 R_O$ or 300 μm. At this location, *without* a flaw, the maximum radial tensile stress is about 285 MPa and a tensile stress gradient develops to a depth of $z \approx 0.075 R_O$ or 75 μm (see fig. 10). Also, the tensile pulse duration near the surface is about 60 ns (see fig. 8 in Section 3).

Figure 10 shows the effect of surface hoop (circumferential) flaws on the *radial* tensile stress gradient ahead of the crack tip for crack depths of 25, 50, and 100 μm ($R_O=1$mm). In each case, the peak radial tensile stress ahead (one-half a cell dimension) of the crack tip is enhanced, but decreases with increasing flaw depth.

---

[4] In fact, an analytic solution by Blowers [6] predicts *infinite* peak tensile stress *at* the impact surface for purely elastic targets.

[5] Note that these elastic solutions can be scaled linearly in dimensions and time for other drop radii as long as the impact velocity and material properties are not changed.
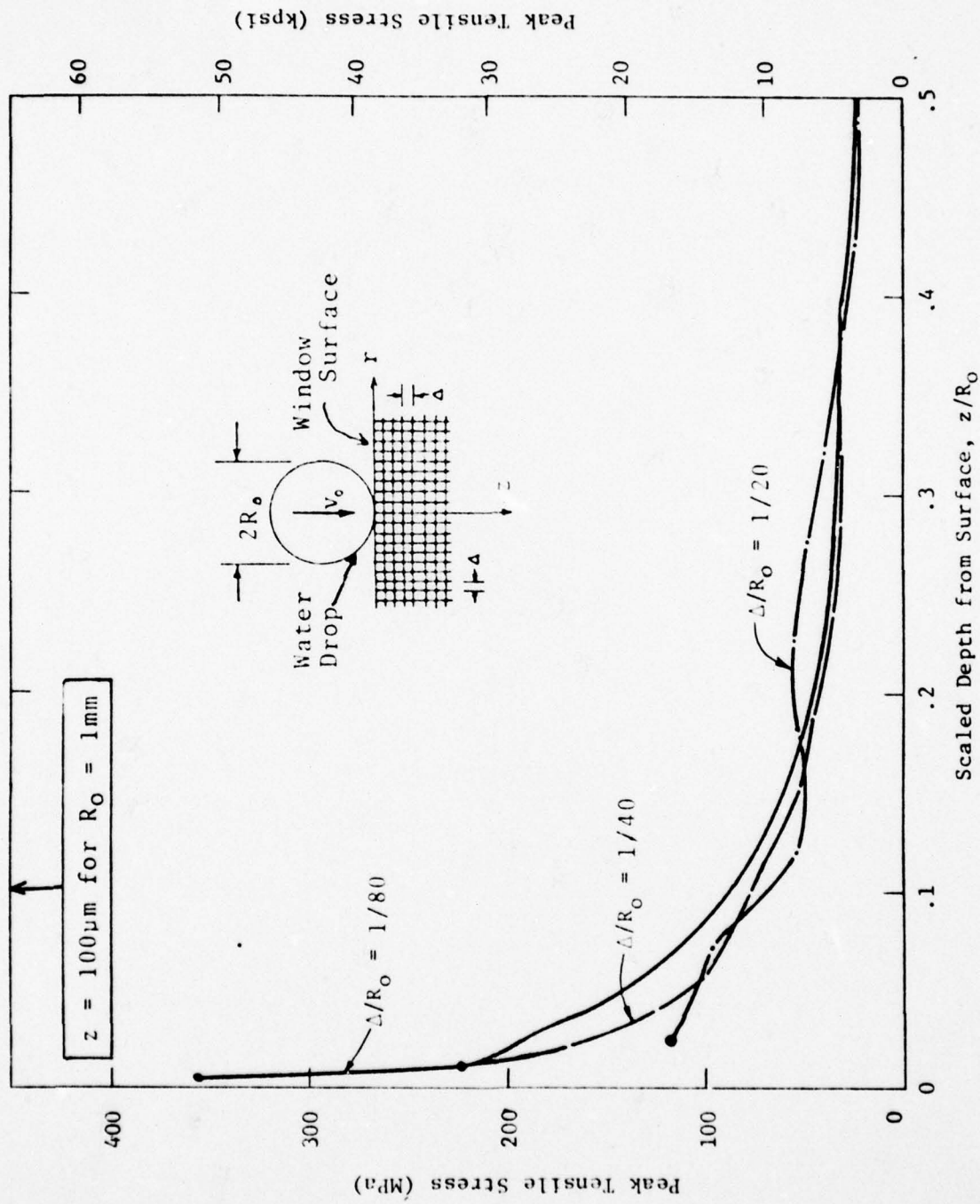
Figure 6. *Peak tensile stress versus depth* (for all radii) in a ZnSe window impacted by a water drop at 222 m/s for variations in computational cell size.
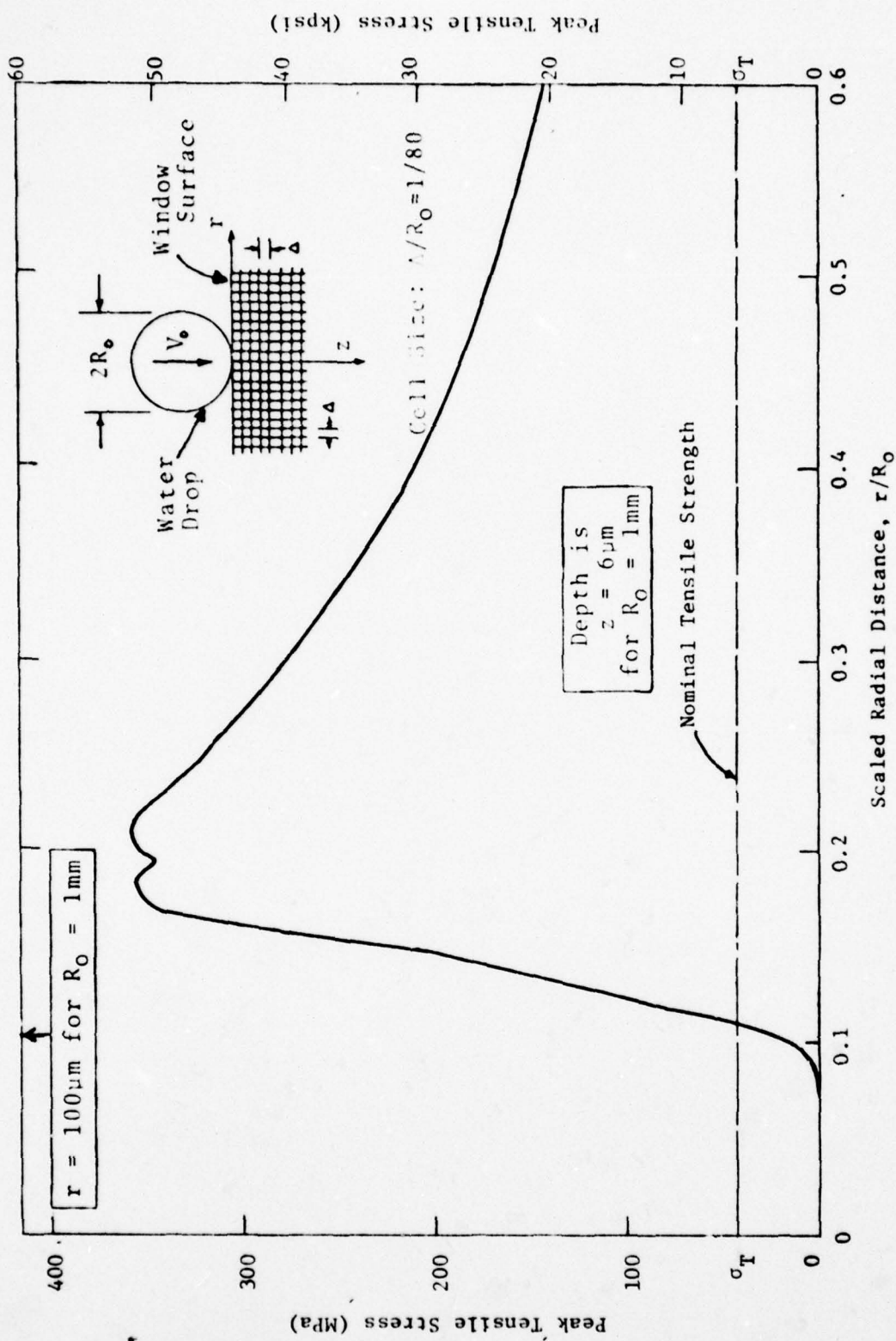
Figure 7. *Peak tensile stress versus radius near the surface* ($z=\Delta/2$) *of a ZnSe window impacted by a water drop at 222 m/s .*
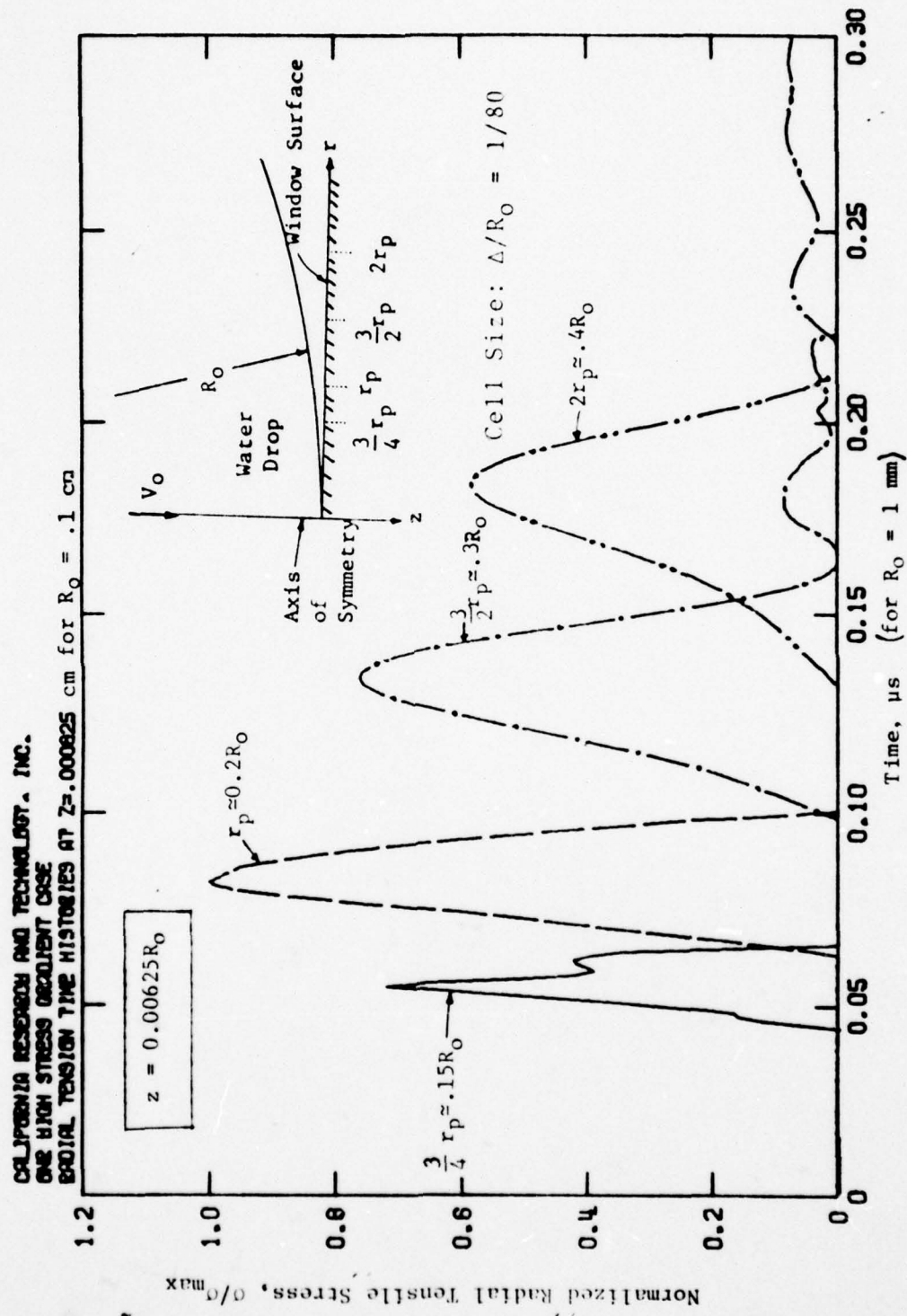
Figure 8. Normalized (σ_{max}=356 MPa at r=rp) *radial tensile stress histories* near surface (z=Δ/2) for impact (V_0=222 m/s) of ZnSe window by a water drop (R_o=1mm).
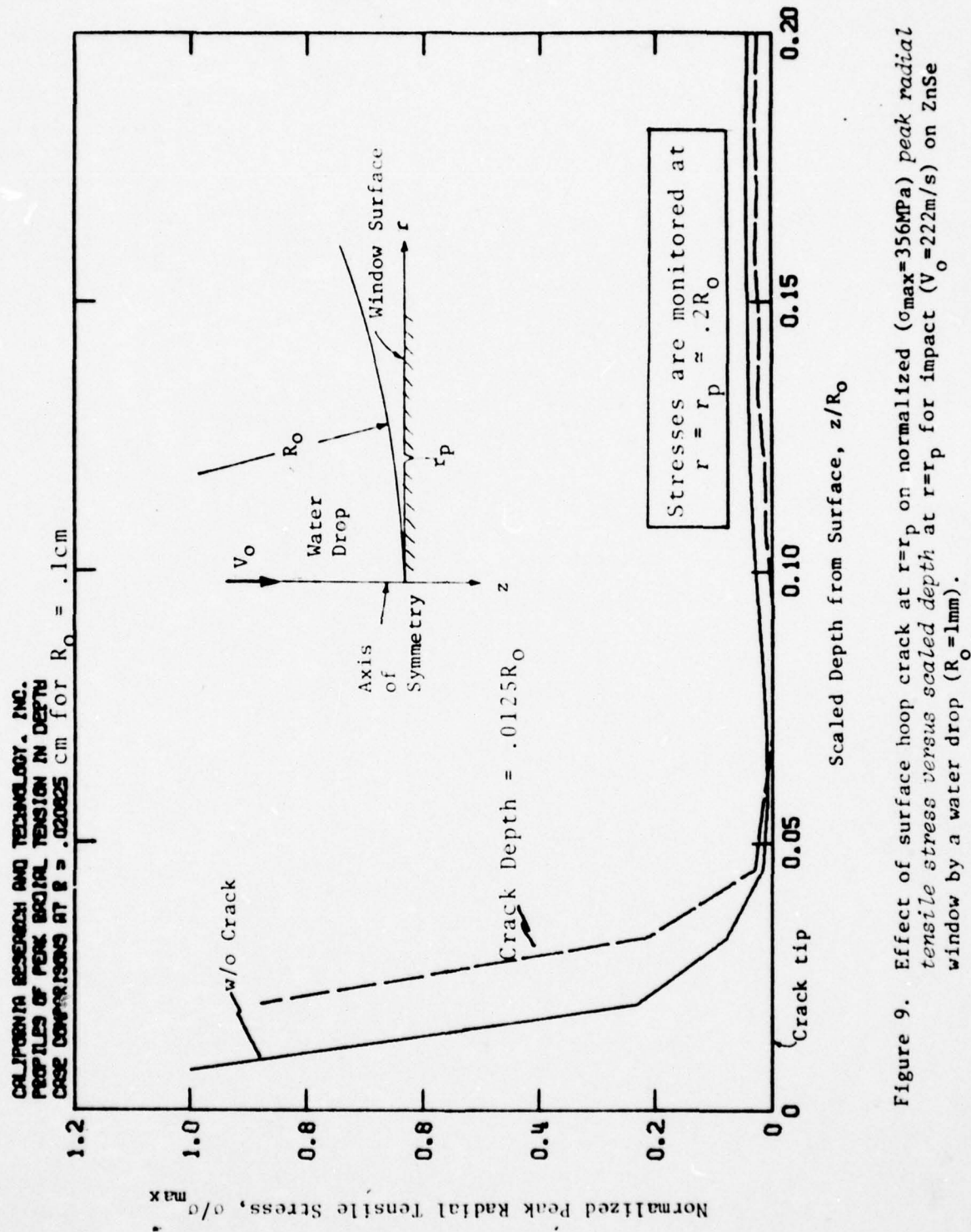
Figure 9. Effect of surface hoop crack at $r=r_p$ on normalized (σ_{max}=356MPa) *peak radial tensile stress versus scaled depth* at $r=r_p$ for impact (V_o=222m/s) on ZnSe window by a water drop (R_o=1mm).
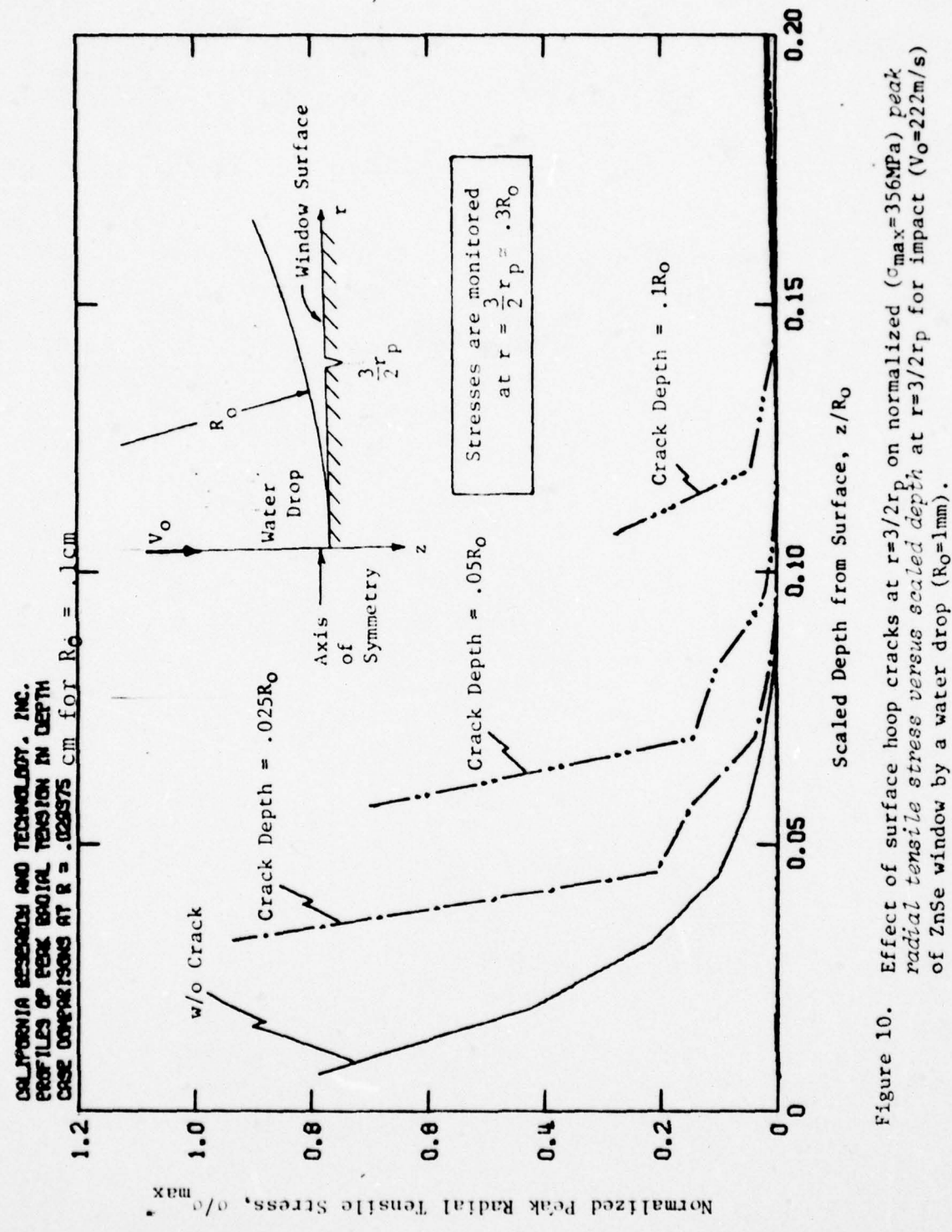
Figure 10. Effect of surface hoop cracks at $r=3/2 r_p$ on normalized ($\sigma_{max}=356MPa$) *peak radial tensile stress versus scaled depth* at $r=3/2 r_p$ for impact ($V_o=222m/s$) of ZnSe window by a water drop ($R_o=1mm$).

Figure 11 shows the effect of the flaws at radius $3/2 \; r_p \approx 0.3 \; R_o$ or 300 μm on the peak radial tensile stress gradient monitored downstream at radius $2 \; r_p \approx 0.4 \; R_o$ or 400 μm. A factor of four reduction (from the no flaw case) is observed near the surface for the 100 μm (R_o=1mm) deep flaw. (Note that the stress profile upstream at $r_p \approx 0.2 \; R_o$ or 200 μm remains essentially unaffected by the flaws.)

5. Discussion

The effects of surface flaws on ceramic target damage from subsonic water drop impacts are investigated using numerical code simulations. The pressure pulse due to water drop impact generates a tensile stress wave with a steep near-surface gradient. Figure 12 shows a schematic view of the effect of a surface flaw on the near-surface tensile stress profile. Upstream profiles remain essentially unchanged, while downstream profiles have reduced gradients and peak value at surface.

Using the stress intensity approach of fracture mechanics, the stress intensity factor, K_I, can be obtained[6], as shown in figure 12, and crack activation is defined by the condition where $K_I \geq K_C$. Figure 13 shows the peak stress intensity factor for various surface flaws based on the results of the crack activation experiments from Section 4 (see fig. 10). For a toughness value of $K_C = 1$ MPa$\sqrt{m}$, surface flaws of depth greater than 75 μm will not propagate.

Thus, as a consequence of the steep stress gradient, surface crack activation under water drop impact is dependent on the depth of surface flaws. In addition, a relatively large surface flaw can perturb the stress field such that crack activation in its vicinity is suppressed.

The authors wish to acknowledge the useful discussions with A. G. Evans of the University of California, Berkeley (formerly at Rockwell International/Science Center).

---

[6] The stress intensity factor is calculated from

$$K_I = \sigma \sqrt{2\pi \frac{\Delta}{2}} = \sigma \sqrt{\pi \Delta}$$

where σ is the radial stress located one-half a cell dimension, $\Delta/2$, from the crack tip.
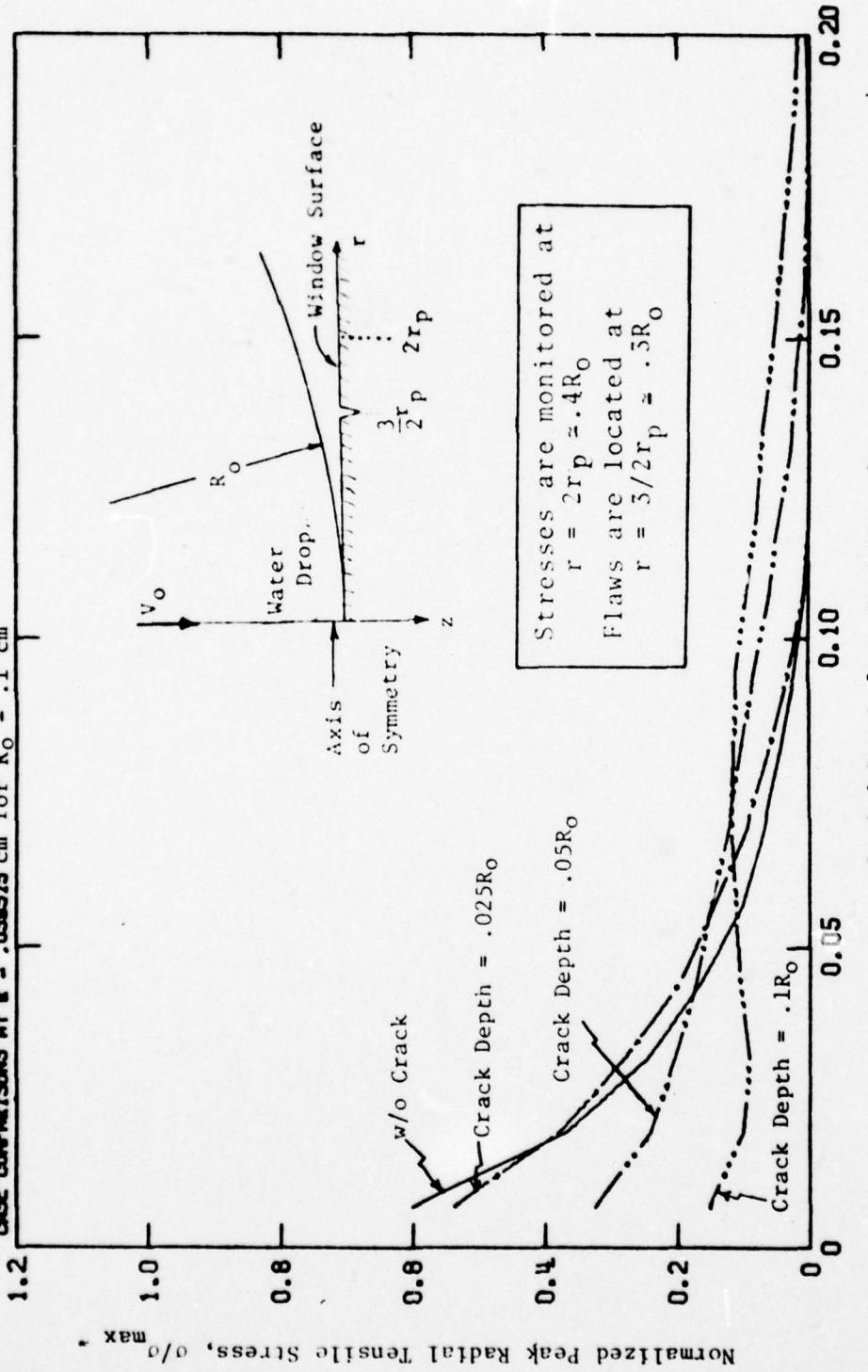
Figure 11. Effect of surface hoop cracks at $r=3/2r_p$ on normalized ($\sigma_{max}= 356MPa$) *peak radial tensile stress versus scaled depth* at $r=2r_p$ for impact ($V_0=222m/s$) of ZnSe window by a water drop ($R_0=1mm$).

Pressure Pulse
Due to Water Drop Impact

Surface

Crack

Downstream
Tensile Stress
Profile Has
Reduced
Gradient

r

c

σ

Δ

Computational
Cell

$K_I = \sigma \sqrt{\pi \Delta}$

Upstream
Tensile Stress
Profile Remains
Essentially
Unchanged

Axis of Symmetry

z
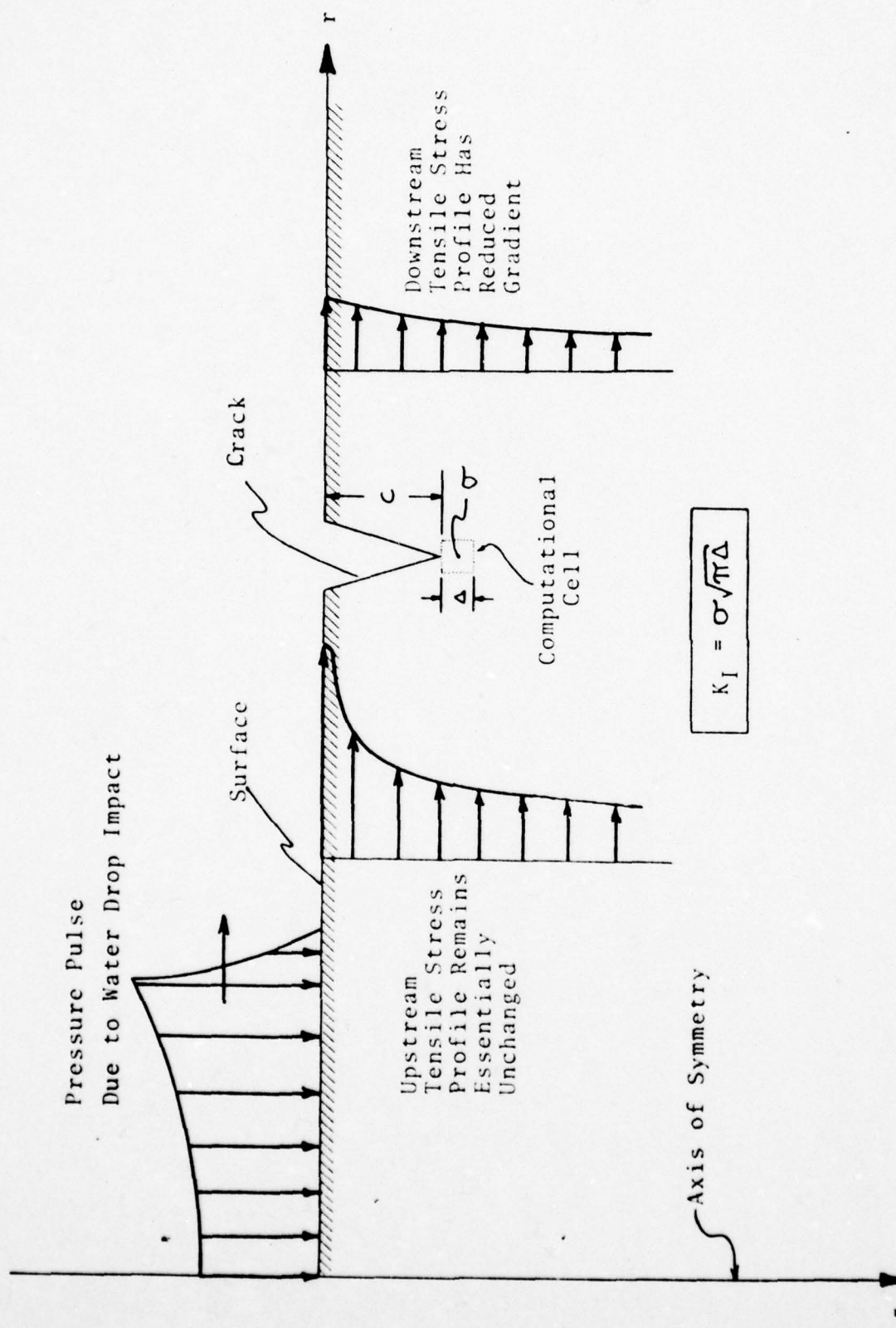
Figure 12. Schematic view of effect of a surface flaw on near surface tensile stress profile and associated stress intensity factor.
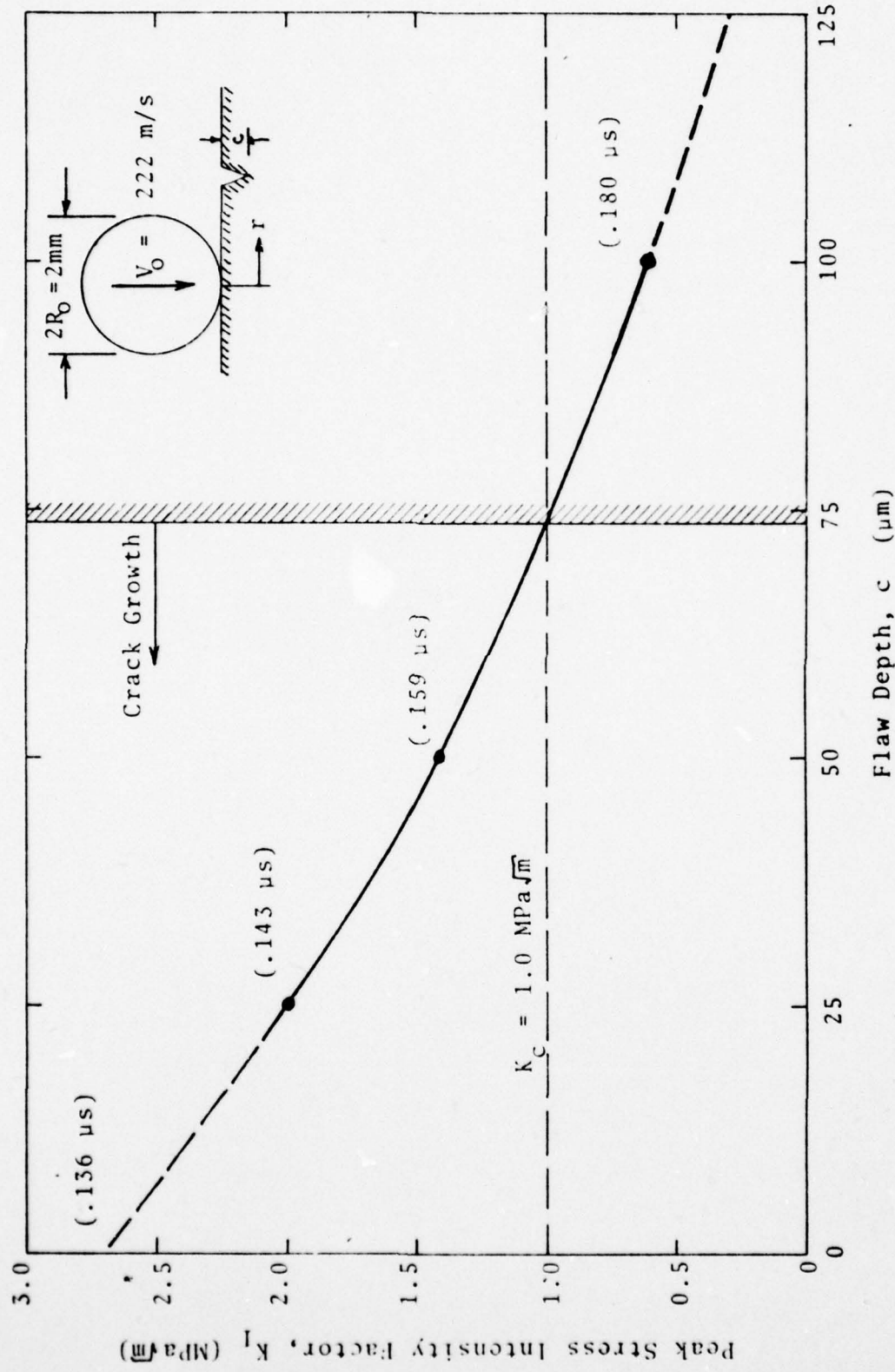
Figure 13. Peak stress intensity factor (and associated time) for various surface flaws located at r=300 μm for 222 m/s impact of a 2-mm water drop onto a ZnSe window.

References

[1] Evans, A. G., Impact damage in ceramics, Report under Office of Naval Research Contract No. N00014-75-C-0609, Rockwell International/Science Center, Thousand Oaks, California (1977).

[2] Wilkins, M. L., Calculation of elastic-plastic flow, Report UCRL-7322, Rev. I, Lawrence Radiation Laboratory, University of California, Livermore, California (1969).

[3] Rosenblatt, M., Eggum, G. E., DeAngelo, L. A., and Kreyenhagen, K. N., Numerical investigation of water drop erosion mechanisms in infrared-transparent materials, Report AFML-TR-76-193, Air Force Materials Laboratory, Wright-Patterson Air Force Base, Ohio (1976).

[4] Kreyenhagen, K. N., Rosenblatt, M., and Isbelle, T. R., Cratering, mass loss, and residual damage due to hypersonic particle impacts on ablative materials, Report AFWL-TR-75-184, Air Force Weapons Laboratory, Kirtland Air Force Base, New Mexico (1976).

[5] Ito, Y. M., Rosenblatt, M., Perry, F. W., and Eggum, G. E., Analysis of water drop erosion mechanisms in infrared-transparent materials using microphysical fracture models, Report AFML-TR-77-219, Air Force Materials Laboratory, Wright-Patterson Air Force Base, Ohio (1977).

[6] Blowers, R. W., On the response of an elastic solid to droplet impact, J. Inst. Maths. Applics. $\underline{5}$, 167-193 (1969).

SECTION II

Effects of Surface Pores in Silicon Nitride
Impacted by a Water Drop

EFFECTS OF SURFACE PORES IN SILICON NITRIDE
IMPACTED BY A WATER DROP

MARTIN ROSENBLATT
LARRY DEANGELO
Y. MARVIN ITO

CALIFORNIA RESEARCH & TECHNOLOGY, INC.
6269 VARIEL AVENUE, SUITE 200
WOODLAND HILLS, CALIFORNIA 91367

DECEMBER 1978

ABSTRACT

A water drop impacting directly on a surface pore
may significantly increase the probability of crack form-
ation and growth near the pore boundary. To examine this
physical process, the dynamics of a 335 m/s water drop
impact on a silicon nitride target with a 40 micron
diameter hemispherical surface pore has been simulated
using a finite difference computer code called WAVE-L.
The numerical simulation solves the finite difference
analogs to the physical conservation equations of mass,
momenta, and energy along with the constitutive equations
for the water and silicon nitride.

Shortly after impact, stress wave dynamics accelerate
the free surface of the water near the axis as this water
flows into the pore. The water on axis impacts the bottom
of the pore with a velocity which is about a factor of 7
higher than the initial impact velocity. This increase in
the water flow velocity and the associated lateral flow of
water into the pore lead to a relatively large pressure
pulse in the pore when the water impacts the bottom of the
pore. A peak compressive pressure of ~60 kbar = 6 GPa is
predicted; this pressure is about a factor of 9 higher than
the 1-D Hugoniot impact pressure.

The maximum tensile stress in the silicon nitride
target is about 15 kbar = 1.5 GPa and occurs at the bottom
of the hemispherical pore on the axis of cylindrical symmetry.
The tensile stresses at the bottom of the pore have a duration
of about 15 ns.

Microstructural failure of the silicon nitride material
near the bottom of the pore appears likely based on the large
predicted tensile stresses and the large predicted stress
intensity factors.

i

EFFECTS OF SURFACE PORES IN A SILICON NITRIDE
TARGET IMPACTED BY A WATER DROP

1. INTRODUCTION

A water drop impacting directly on a surface pore may significantly increase the probability of crack formation and growth near the pore boundary. To examine this physical process, the dynamics of a 335 m/s water drop impact on a silicon nitride target with a 40 micron diameter hemispherical pore has been calculated. This pore size is representative for reaction bonded Si_3N_4 (Reference 1). The pore diameter is small compared to millimeter size water drops of interest; thus, the water boundary is assumed to be a flat surface, as indicated in Figure 1. The stress wave dynamics between the water drop and silicon nitride target are simulated using a finite difference computer code called WAVE-L. WAVE-L is a Lagrangian code of the HEMP type (Ref. 2). The numerical simulation solves the finite difference analogs to the physical conservation equations of mass, momenta, and energy along with the constitutive equations for the water and porous silicon nitride. The water is treated as a compressible inviscid fluid while the silicon nitride is treated as linear elastic. The material properties for these materials are indicated on Figure 1; the detailed equation of state for water can be found in Reference 3.

The basic physical response of the water and target material near the pore is described in Section 2. The *dynamic tensile stress characteristics* in the target, which provide the driving forces for crack initiation and growth, are described in Section 3. In Section 4, the conclusions are presented and discussed.

1

2. THE WATER DROP AND TARGET DYNAMICS NEAR THE SURFACE PORE

Figure 2 shows the initial computational grid configuration. The left axis is an axis of cylindrical symmetry. The explicitly defined hemispherical surface flaw is treated as a void in this numerical simulation. The computational cells have been zoned to provide a good definition of stresses near the boundary of the surface flaw. Stresses are calculated at all cell centers, while particle velocities are calculated at all cell corners. Note that the water can slide over the surface of the porous silicon nitride target. The sliding interfaces are considered frictionless. The sliding occurs both along the hemispherical boundary of the surface pore as well as on the flat front surface of the target near the pore.

Figure 3 shows a particle velocity (left half) and principal stress (right half) field plot at 8 nanoseconds (ns) after impact. The velocity vectors and three principal stresses are plotted for both the water and Si_3N_4 directly from the numerical simulation. Scale bars for the magnitude of the vectors and stress components are indicated at the top of the field plots. Also, a description of the principal stress conventions is shown.

The velocity flow field at 8 ns shows the downward and lateral flow of water into the pore. The lateral flow into the pore is a direct consequence of the large stress gradients which form in the water upon impact. Upon impact, the 1-D Hugoniot stresses (P = 6.8 kbar = 680 MPa) develop near the interface between the water and silicon nitride target. However in the region of the pore, the water does not impact any target material and therefore no pressures initially develop. The initial pressure gradient at r = 20 μm in the water causes pressure waves to propagate toward the axis of cylindrical symmetry and causes inward radial velocities to develop in the water.

2

The very high wave velocities in the silicon
nitride target cause the entire pore boundary to be stressed
very early (~3 ns). Note that by 8 ns stress waves in the
target have propagated to depths of about .008 cm = 80 μm
which is relatively large compared to the pore depth of
20 μm.

Figure 4 shows the velocity and principal stress field
at 15 ns. Note the relatively large volume of water which
has now achieved inward radial velocities. The peak free
surface water velocity in the pore is now 82% higher than
the initial impact velocity. In the silicon nitride target,
the particle velocities are very low due to the much higher
impedance (ρC_o) in the target as compared to the water.
Figure 5 shows the corresponding plot at 23 ns. By this time,
the water along the boundary of the pore has moved over half
way down the pore. The peak particle velocity of the water
is now 150% higher than the initial impact velocity.

Figure 6 shows the velocity and principal stress field
plots at 30 ns after impact with the target surface. At
this time, the water has almost completely filled the pore
with only a small volume near the pore bottom remaining as
void. (Notice that the effects of compression of the air
initially filling the pore have been ignored in this calcula-
tion). The velocities near the axis are now quite large, a
factor of ~4 greater than the initial velocity. Note that
both the velocity and stress scale bars have been changed in
this plot due to the large spatial field of view. The
stresses in the target near the pore are in tension at the
bottom of the pore at this time. In the next section these
tensions will be shown to reach ~15 kb = 1500 MPa = 1.5 GPa.

At 33 ns (Figure 7) the water impacts the bottom of the
pore and a strong compressive pulse is generated in the water
and in the target near the bottom of the pore. The impact

3

velocity of the water on the pore bottom is a factor of ~7 greater than the initial impact velocity. The peak compressive pressure is ~60 kbar = 6,000 MPa. The pressures propagate through the water in the pore and begin to reverse the flow of the water as shown on Figure 8, t = 38 ns. By 53 ns (Figure 9), water is flowing out of the pore.

3. MAXIMUM PRINCIPAL TENSILE STRESS HISTORIES IN THE POROUS SILICON NITRIDE TARGET

During the numerical simulation, several target locations were monitored for principal stress histories. Figures 10 through 16 show the maximum principal tensile stress histories near the pore boundary at several stations in the linear elastic target. The following sketch shows the relevant target locations.

Station	Ψ
1	0
2	26°
3	49°
4	90°

	Z
7	1.4R
9	1.7R
10	2.4R

axis

R = 20 μm

Ψ

Z

Si$_3$N$_4$, Silicon Nitride Target
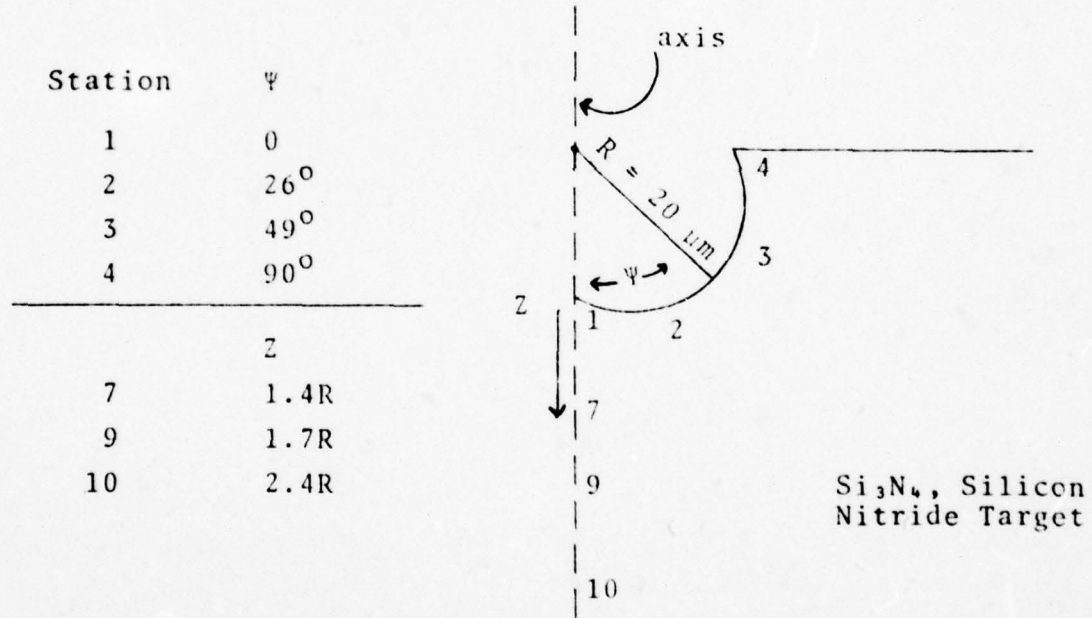
Figure 10 shows the tension history at Station 1 at the bottom of the pore on the axis of cylindrical symmetry. (A sketch appears on each figure showing the location of the monitored stresses.) The key reference time is t = .033 μs = 33 ns which is when the water impacts the bottom of the

4

pore. The greatest tension calculated anywhere in the target is 15 kbar = 1.5 GPa which develops at Station 1 shortly after water impacts the bottom of the pore. However, the tensile stress history at the bottom of the pore shows large tensile stresses of nearly the same magnitude forming just prior to t = 33 ns. Then, when the water impacts the bottom of the pore, a compressive stress wave begins to propagate into the target and the principal stresses near the bottom of the pore are all compressive*. Once this compressive stress pulse propagates and attenuates in the target, the relatively high pressures present in the water filling the pore cause large "hoop" tensile stresses near the bottom of the pore. These tensile stresses have a duration of about 15 ns.

Figure 11 shows the maximum tensile stress history at Station 2 (ψ = 26° near the pore surface). Also, on this figure and the other tensile stress histories, the Station 1 results are shown for reference. The tensile stresses do not get as high or last as long off the axis of cylindrical symmetry as on the axis.

Figure 12 shows the tensile stress history at Station 3, ψ = 49°. Figure 13 shows the tensile stress history at Station 4, ψ = 90°. No significant tension develops at this station.

Figures 14, 15 and 16 show the tensile stress histories at axial Stations 7, 9 and 10, respectively. note that the peak tension decays rapidly with depth. By Z = 2.4R, the peak tension is reduced to ~2 kbars = 200 MPa and has a duration of ~2 ns.

Figure 17 shows a comparison of the numerical simulation stress predictions on the pore surface at t = 45 ns with a simple "steady state" analytical model. This comparison was

---

* The value plotted in Figure 10 is the least compressive principal stress.

5

performed to provide partial validation of the numerical simulation results for this configuration. The analytical model is composed of a superposition of two solutions found in Timoshenko (Ref. 4, pages 392-398). The two solutions are combined to attain a uniaxial strain far field boundary condition. The uniform internal pressure component was selected to approximate the water pressure in the pore. The comparisons are very good, especially near the axis of symmetry ($\Psi = 0$) where the relatively high water pressure in the pore dominates the formation of the hoop tension ($\sigma_{\Psi\Psi}$) and radial compression (σ_{rr}).

4. CONCLUSIONS

Based on the numerical simulation results, the following conclusions are presented for a hemispherical surface pore in silicon nitride impacted at 335 m/s by a water drop:

1. The maximum tensile stress in the silicon nitride target is about 15 kbar = 1.5 GPa and occurs at the bottom of the hemispherical pore on the axis of cylindrical symmetry. The tensile stresses at the bottom of the pore have a duration of about 15 ns.

2. Stress wave dynamics accelerate the water near the axis as this water flows into the pore. The water on axis impacts the bottom of the pore with a velocity which is about a factor of 7 higher than the initial impact velocity. This increase in the water flow velocity and the associated lateral flow of water into the pore lead to a relatively large pressure pulse in the pore when the water impacts the bottom of the pore. A peak compressive pressure of ~60 kbar = 6 GPa is predicted; this pressure is about a factor of 9 higher than the 1-D Hugoniot impact pressure.

3. Microstructural failure of the silicon nitride material near the bottom of the pore appears likely based on the following two considerations. First, there is a reported static tensile strength of 79-141 MPa (Ref. 1) which is an order of magnitude lower than the predicted dynamic tensile stresses. Second, the "effective" stress intensity factor exceeds the measured K_{IC}. Note that a stress intensity factor cannot be rigorously defined for the ideal hemispherical pore, since there is no crack tip. However, the following sketch and first order relationship represent an approximation for the effective stress intensity factor on a small crack located at the bottom of the pore.

6

Pore

Si$_3$N$_4$

Z_p
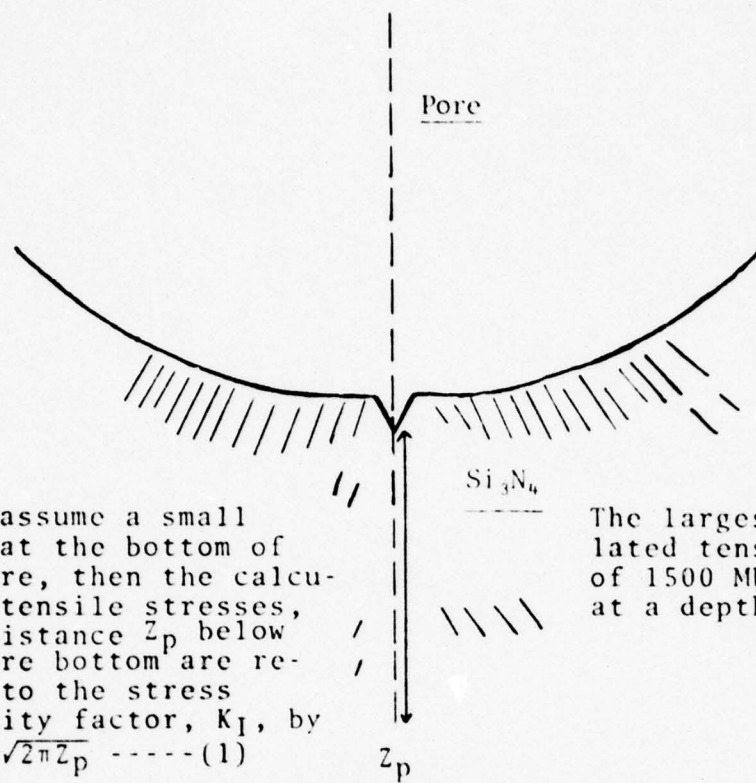
If we assume a small crack at the bottom of the pore, then the calculated tensile stresses, σ, a distance Z_p below the pore bottom are related to the stress intensity factor, K_I, by

$$K_I \sim \sigma\sqrt{2\pi Z_p} \quad -----(1)$$

The largest calculated tensile stress of 1500 MPa occurred at a depth of $Z_p = 2$ μm.

Using $\sigma = 1500$ MPa and $Z_p = 2$ μm in Equation 1 to obtain an approximate value for the maximum predicted stress intensity factor, we find $K_I^{max} \sim 5$ MPa·m$^{\frac{1}{2}}$ which is greater than the reported critical stress intensity factor of $K_{IC} = 2-4$ MPa·m$^{\frac{1}{2}}$ for reaction bonded Si$_3$N$_4$ (Ref. 1).

A numerical simulation approach to crack initiation, propagation and arrest for water drop impacts on ceramics can be found in References 5 and 6. This general dynamic crack growth approach should be applied to predict crack growth characteristics near a surface pore subjected to water drop impacts.

REFERENCES

1. J. W. Edington, D. S. Rowcliffe and J. L. Henshall, "The Mechanical Properties of Silicon Nitride and Silicon Carbide: Parts 1 and 2", Powder Metallurgy International, Vol. 7, Nos. 2 and 3, 1975.

2. M. L. Wilkins, "Calculation of Elastic-Plastic Flow", UCRL-7322 Rev. 1, January 1969.

3. W. A. Walker and H. W. Sternberg, "The Chapman-Jouguet Isentrope and the Underwater Shockwave Performance of Pentolite", The Fourth Symposium on Detonation, Naval Ordinance Laboratory, White Oak, Md., 12-15 October 1965, pp. 27-38.

4. S. P. Timoshenko and S. N. Goodier, Theory of Elasticity, McGraw-Hill Book Company, Third Edition, 1970.

5. M. Rosenblatt, G. E. Eggum, L. A. DeAngelo and K. N. Kreyenhagen, "Numerical Investigation of Water Drop Erosion Mechanisms in Infrared-Transparent Materials", AFML-TR-76-193, December 1976.

5. Y. Marvin Ito, Martin Rosenblatt, Fred W. Perry and Gordon E. Eggum, "Analysis of Water Drop Erosion Mechanisms in Infrared-Transparent Materials Using Microphysical Fracture Models", AFML-TR-77-219, October 1977.

Water V_0 = 335 m/s=1100 ft/s

Porous Silicon Nitride

axis of symmetry

40 μm

LINEAR ELASTIC

COMPRESSIBLE HYDRODYNAMIC EQUATION OF STATE

$P = P(\rho, e)$
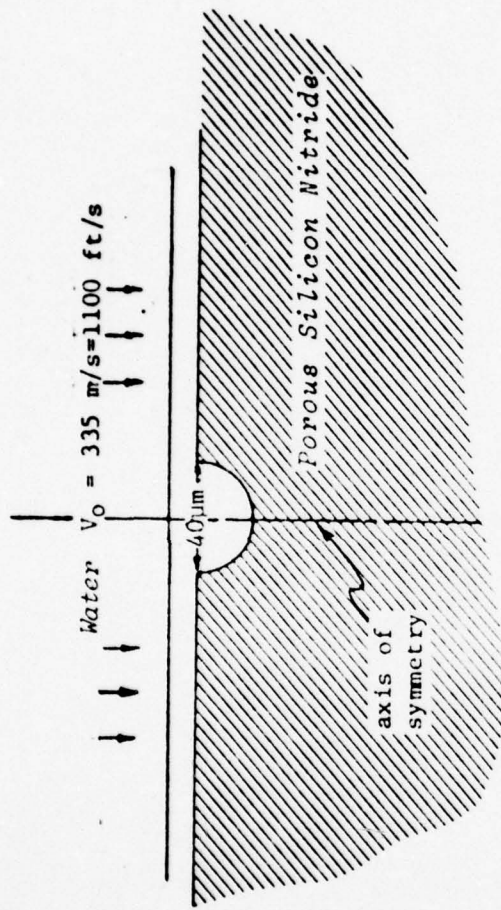
MATERIAL PROPERTIES

	ρ_0 (GM/CM^3)	ν	E (GPA)	K (GPA)	C_D (KM/S)
SILICON NITRIDE	2.7	.25	230	153	10
WATER	1	.5	0	2.3	1.5

Figure 1. Problem Definition and Material Properties.

9
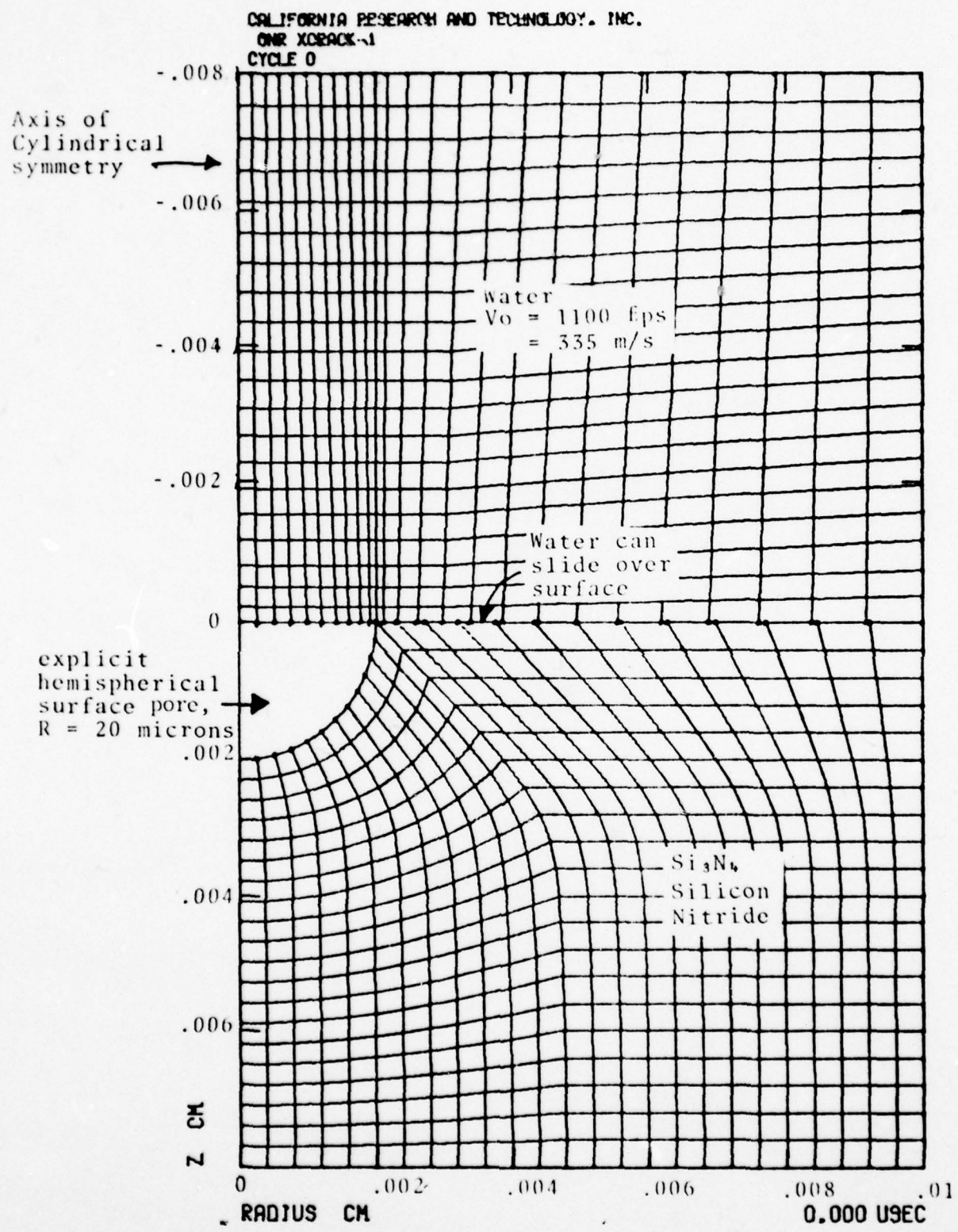
Figure 2. Computational Grid Configuration at Initial Condition.
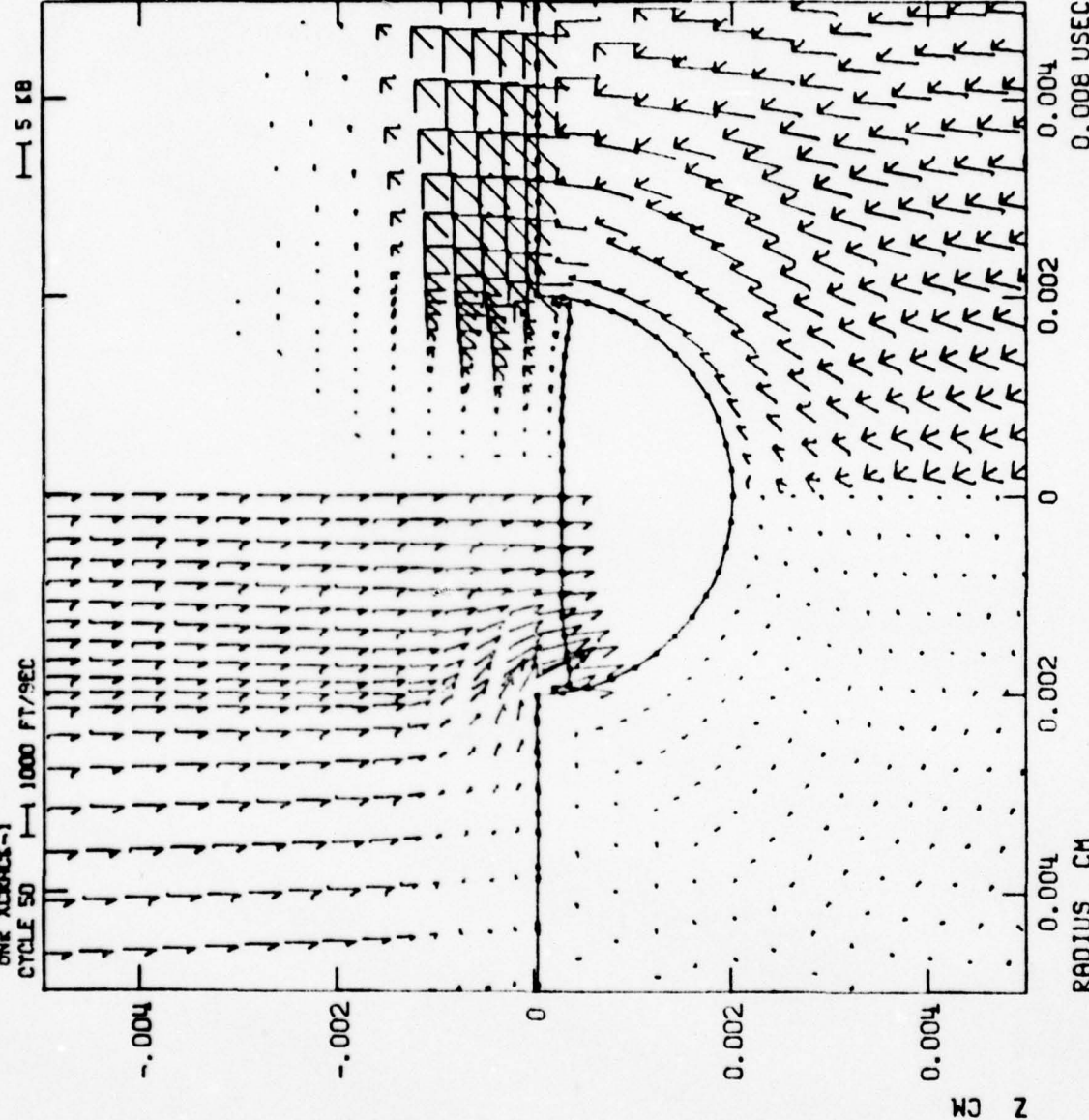
Figure 3. Particle Velocity and Principal Stress Fields at 8 Nanoseconds for an 1100 fps (335 m/s) Water Drop Impact on a 40μm Diameter Pore in Silicon Nitride.

11
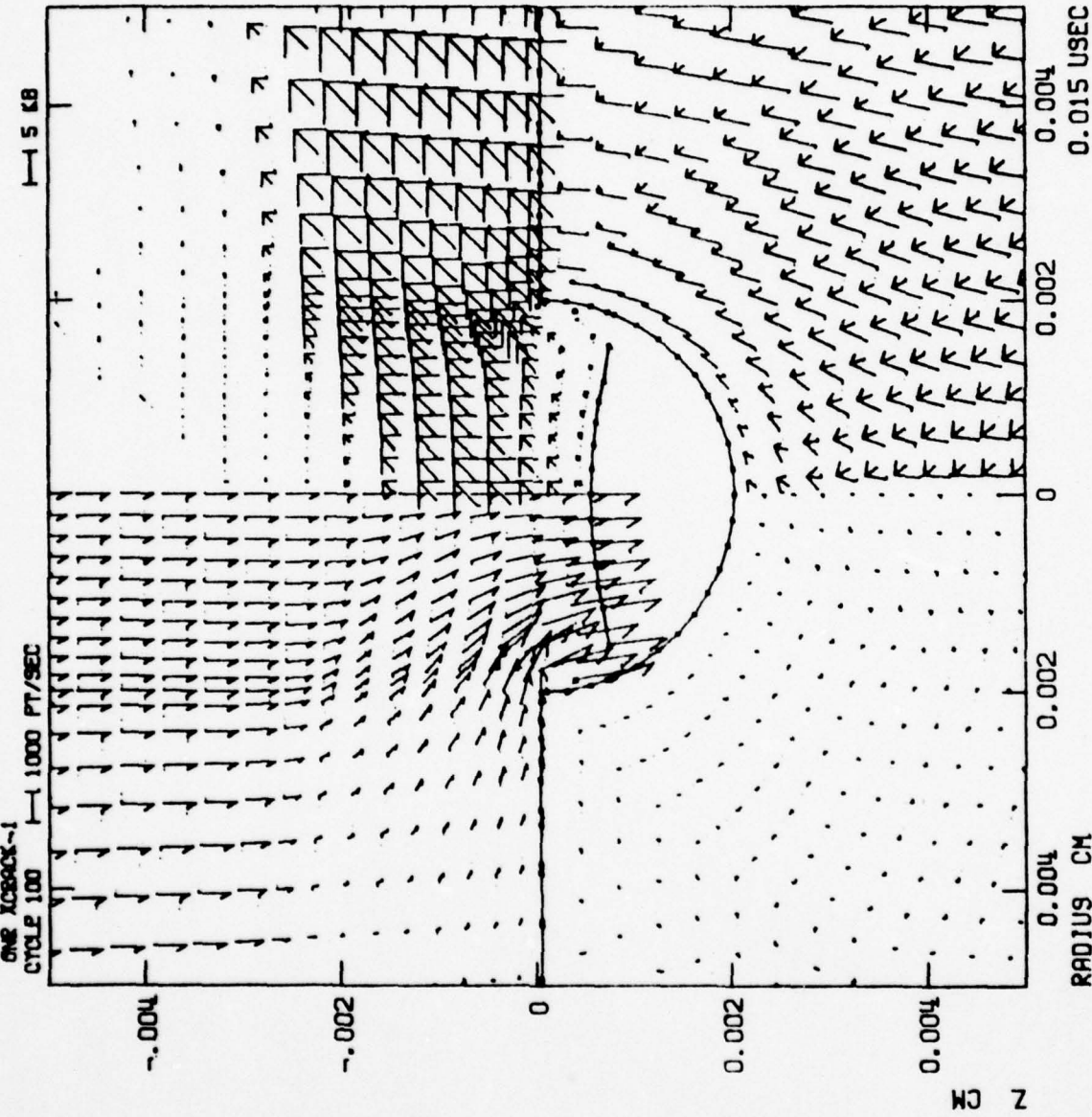
Figure 4. Particle Velocity and Principal Stress Fields at 15 Nanoseconds for an 1100 fps (355 m/s) Water Drop Impact on a 40μm Diameter Pore in Silicon Nitride.

12
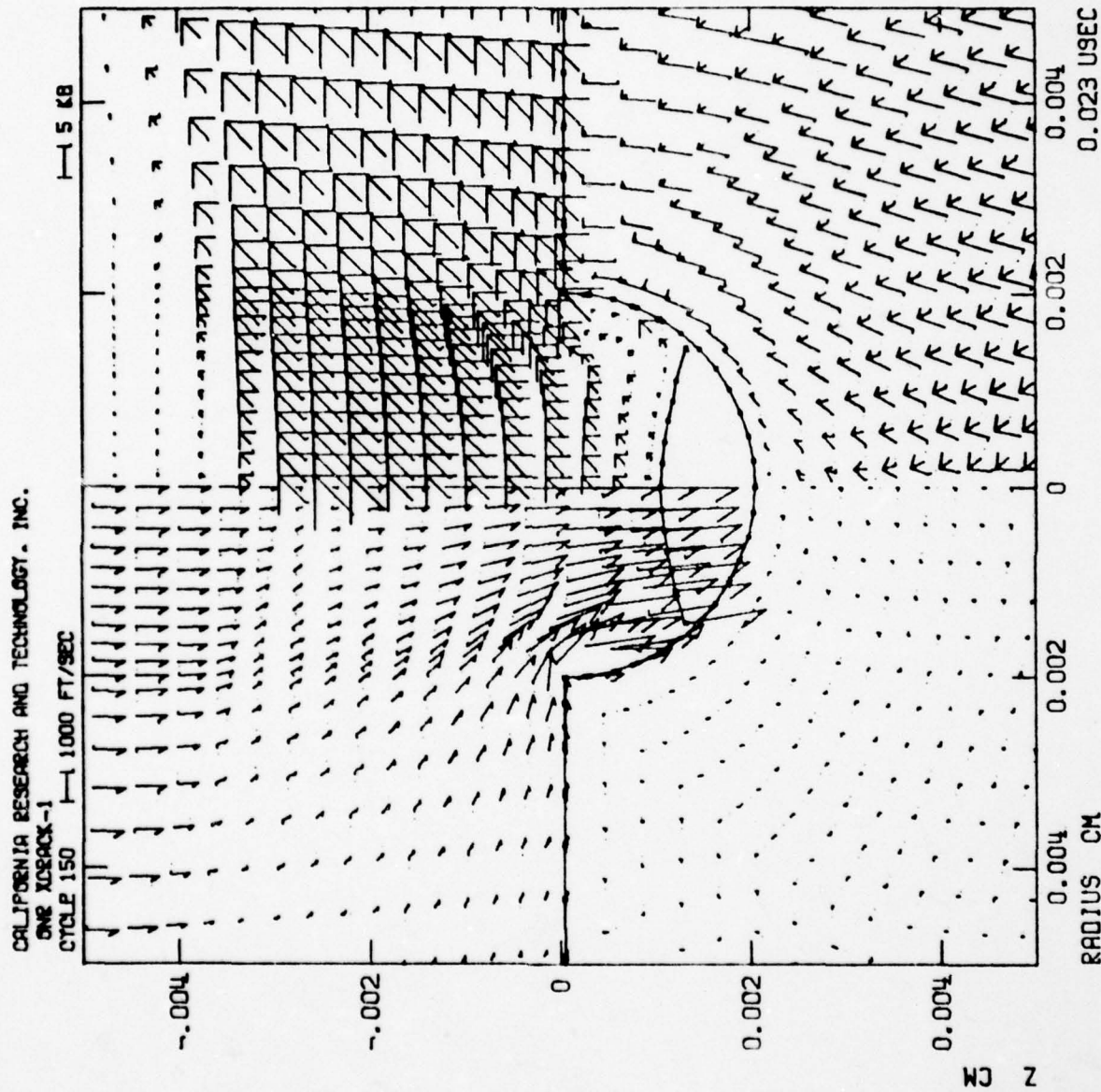
Figure 5. Particle Velocity and Principal Stress Fields at 23 Nanoseconds for an 1100 fps (335 m/s) Water Drop Impact on a 40μm Diameter Pore in Silicon Nitride.
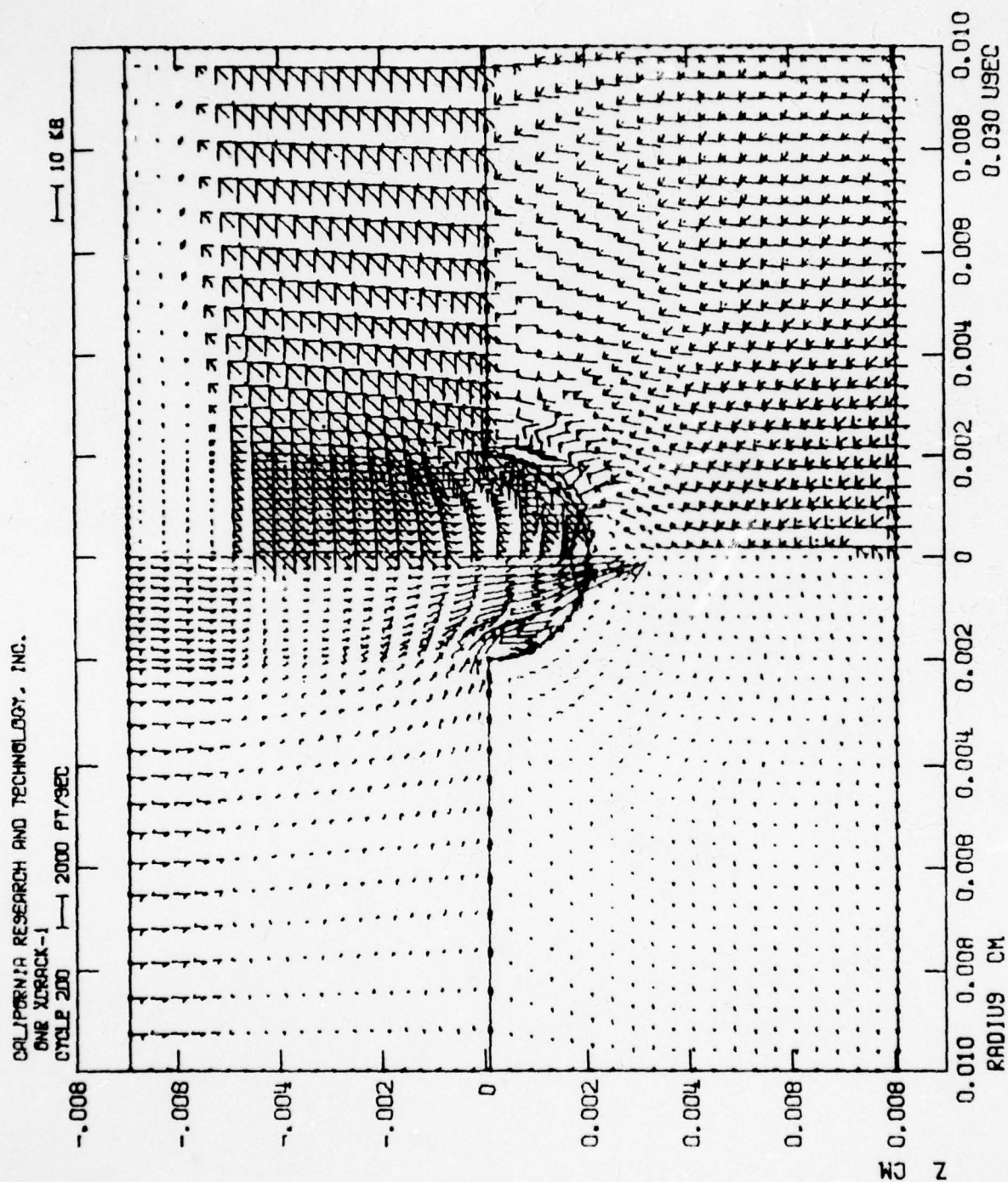
Figure 6. Particle Velocity and Principal Stress Fields at 30 Nanoseconds for an 1100 fps (335 m/s) Water Drop Impact on a 40μm Diameter Pore in Silicon Nitride.

14
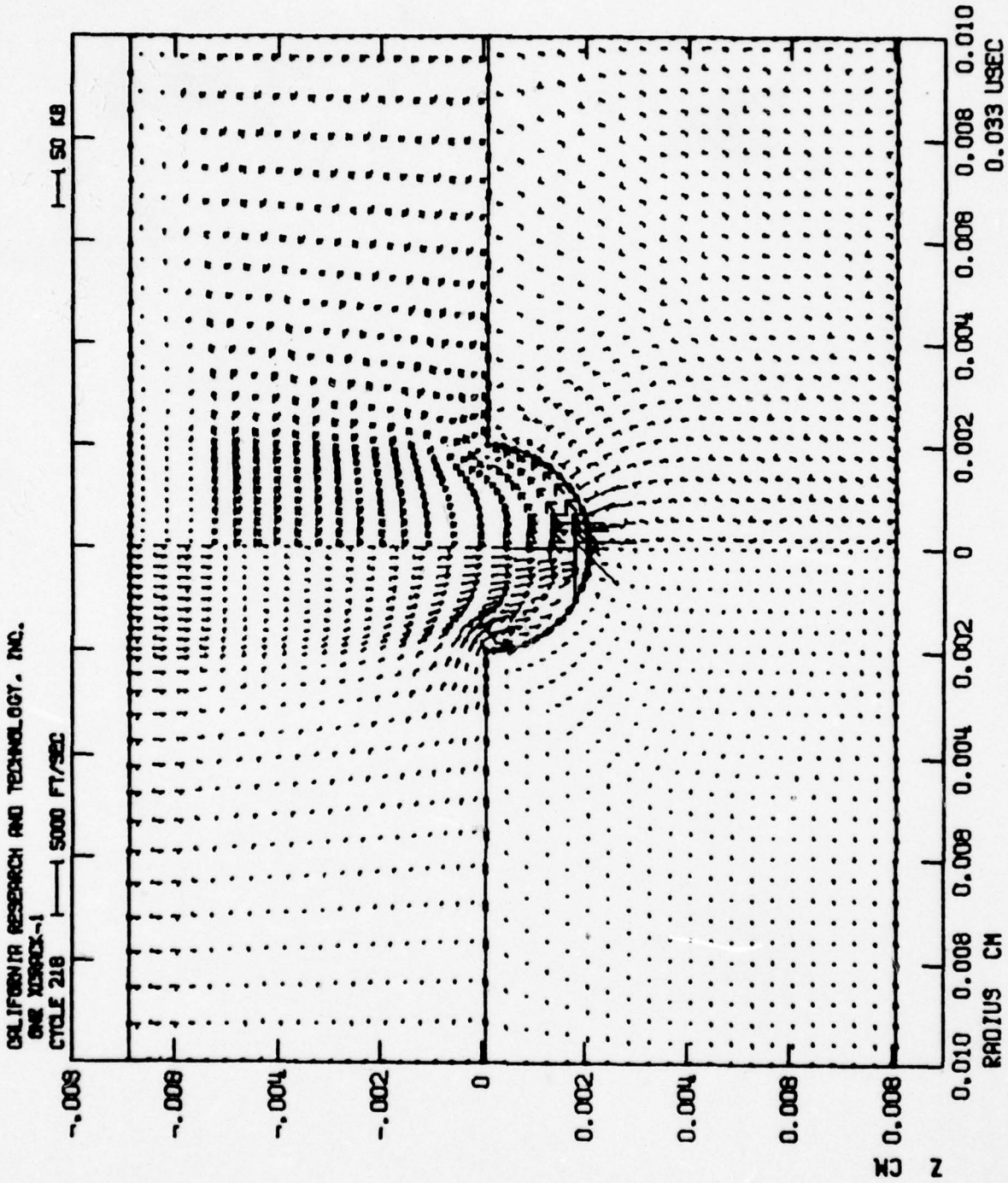
Figure 7. Particle Velocity and Principal Stress Fields at 35 Nanoseconds for an 1100 fps (335 m/s) Water Drop Impact on a 40μm Diameter Pore in Silicon Nitride.

15
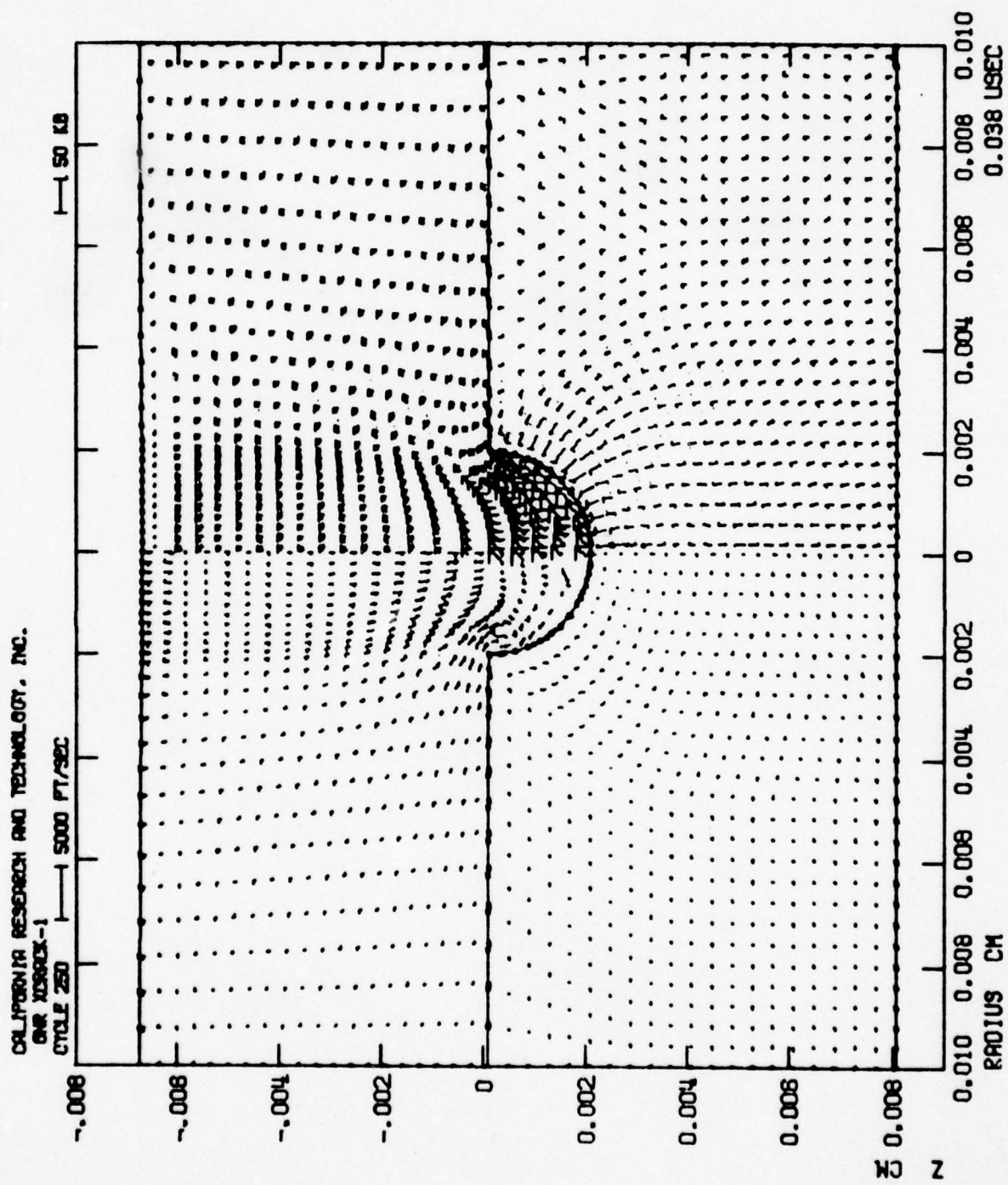
Figure 8. Particle Velocity and Principal Stress Fields at 38 Nanoseconds for an 1100 fps (335 m/s) Water Drop Impact on a 40µm Diameter Pore in Silicon Nitride.

16
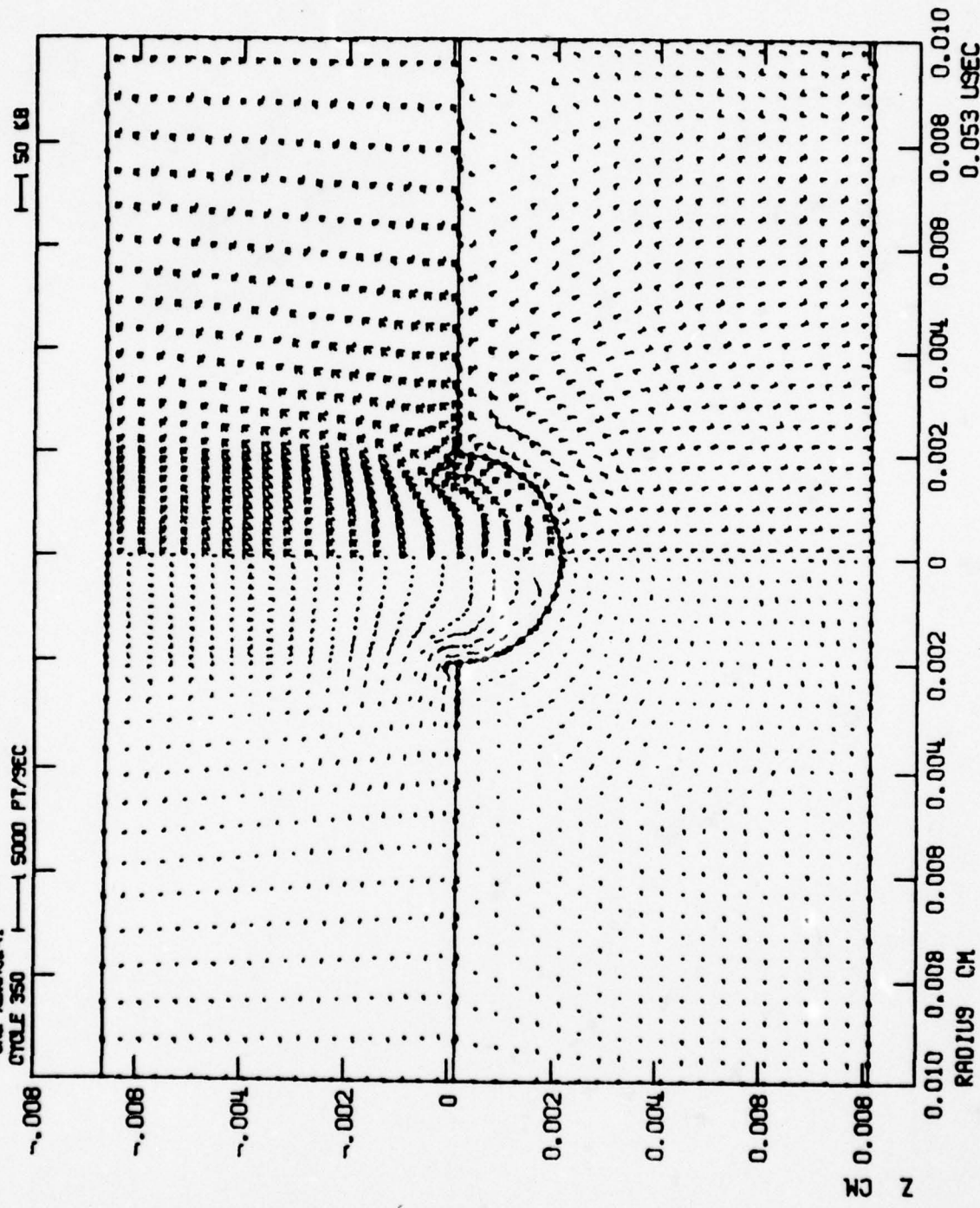
Figure 9. Particle Velocity and Principal Stress Fields at 53 Nanoseconds for an 1100 fps (335 m/s) Water Drop Impact on a 40μm Diameter Pore in Silicon Nitride.
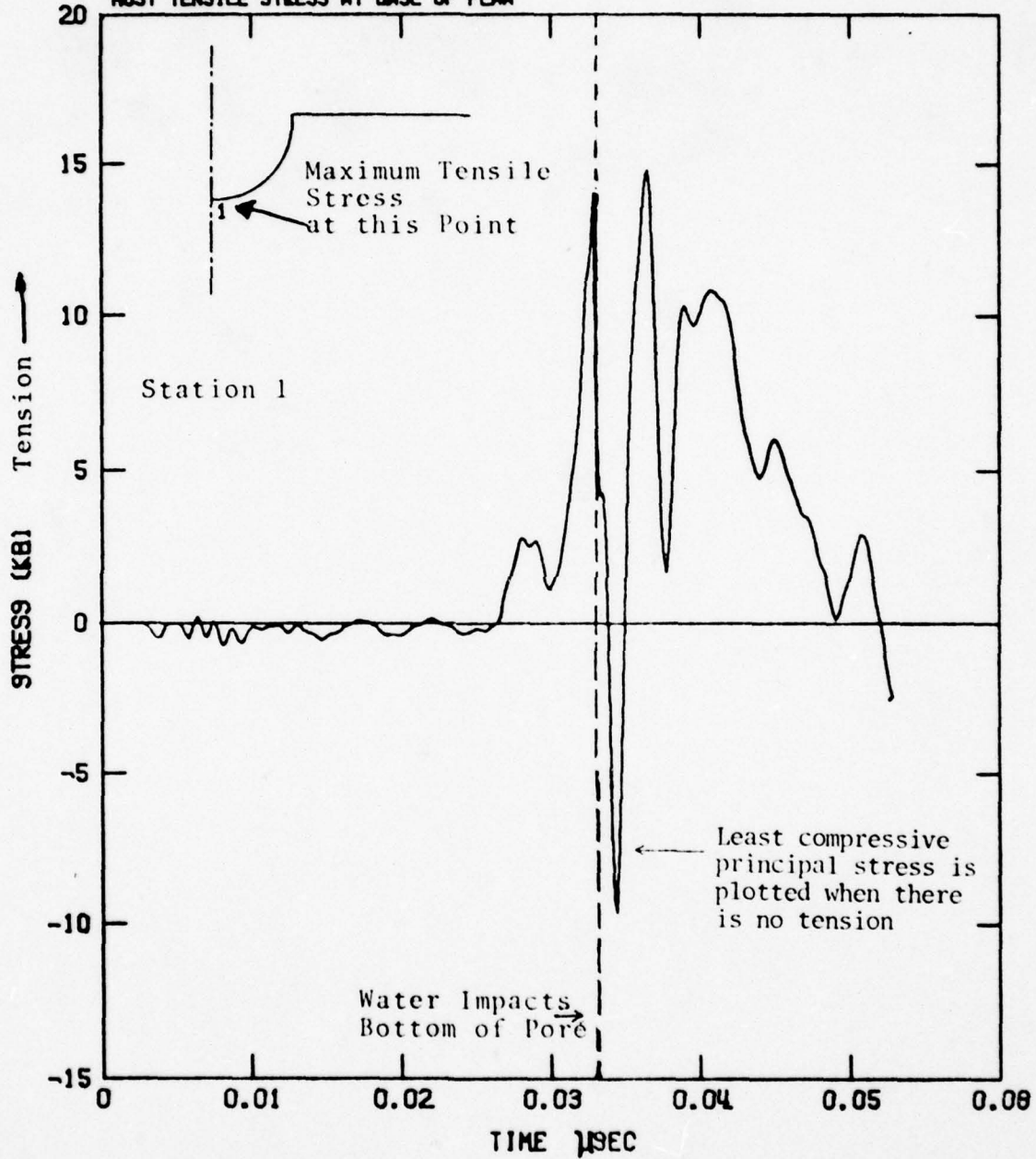
Figure 10. Maximum Principal Tensile Stress versus time at Base of 40μm Diameter Pore (1kb = 100MPa).
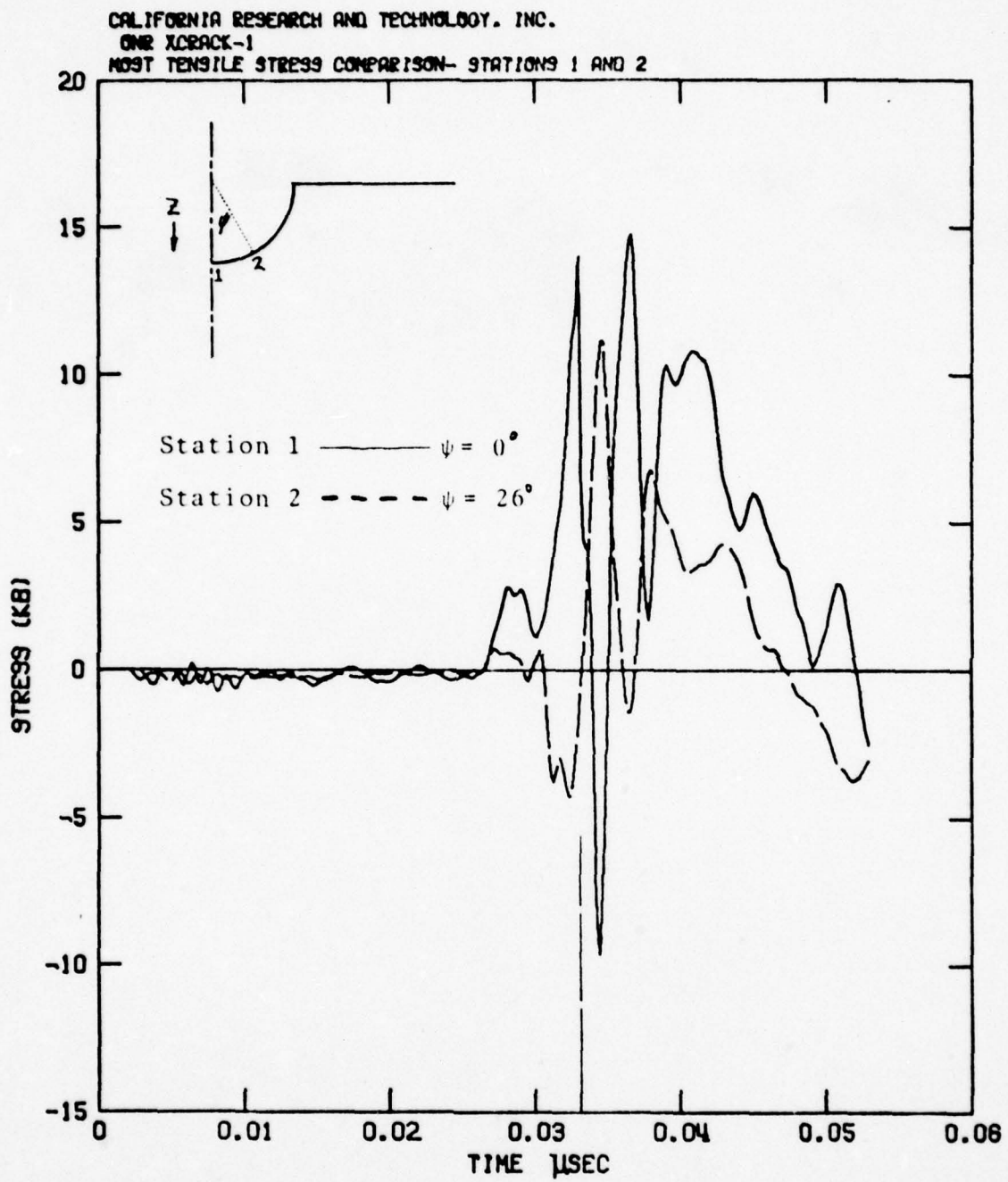
Figure 11.   Comparisons of Maximum Principal Tensile Stress versus
Time at Indicated Station (1kb = 100MPa)

19
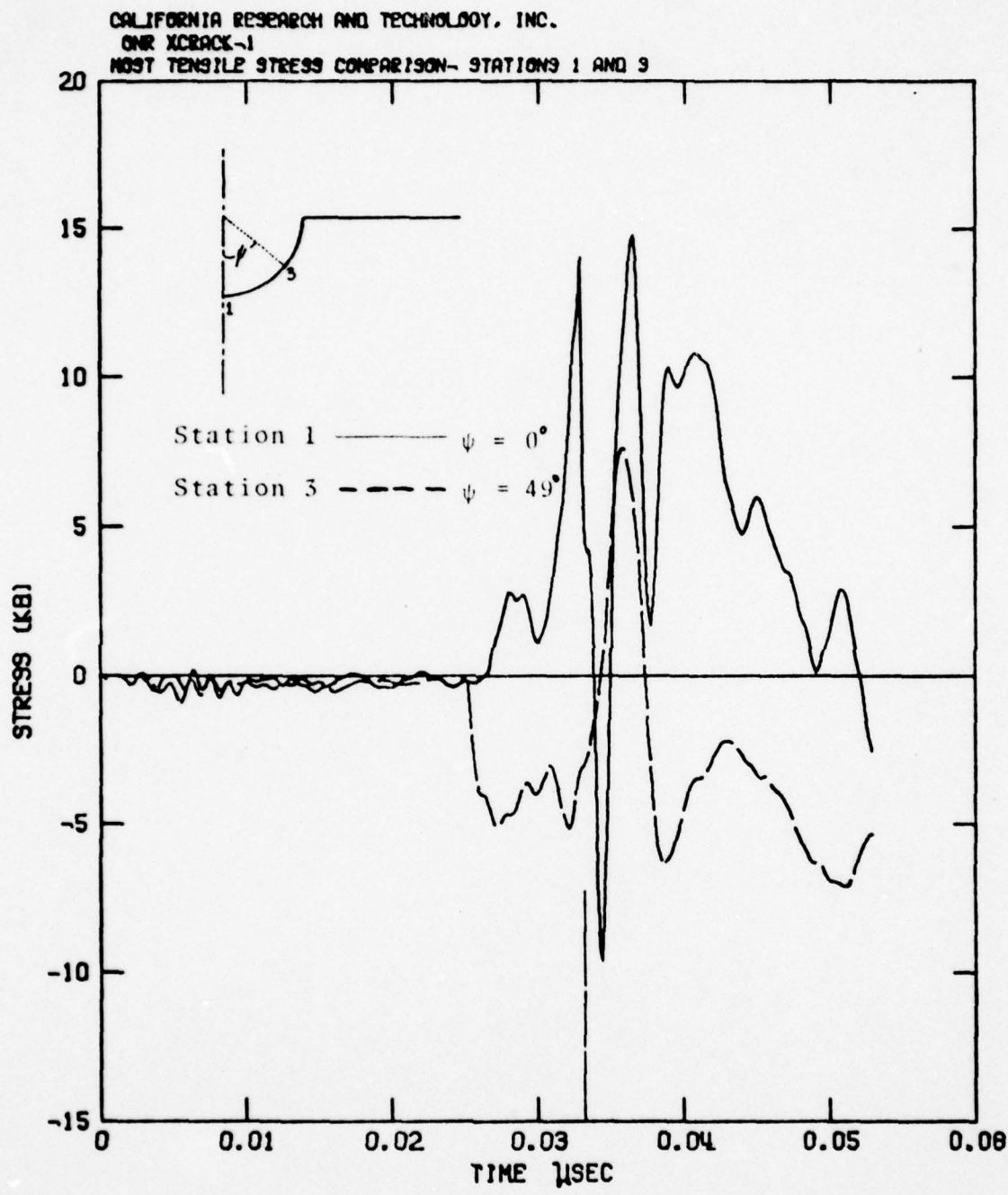
Figure 12. Comparisons of Maximum Principal Tensile Stress versus
Time at Indicated Station (1kb = 100MPa)

20
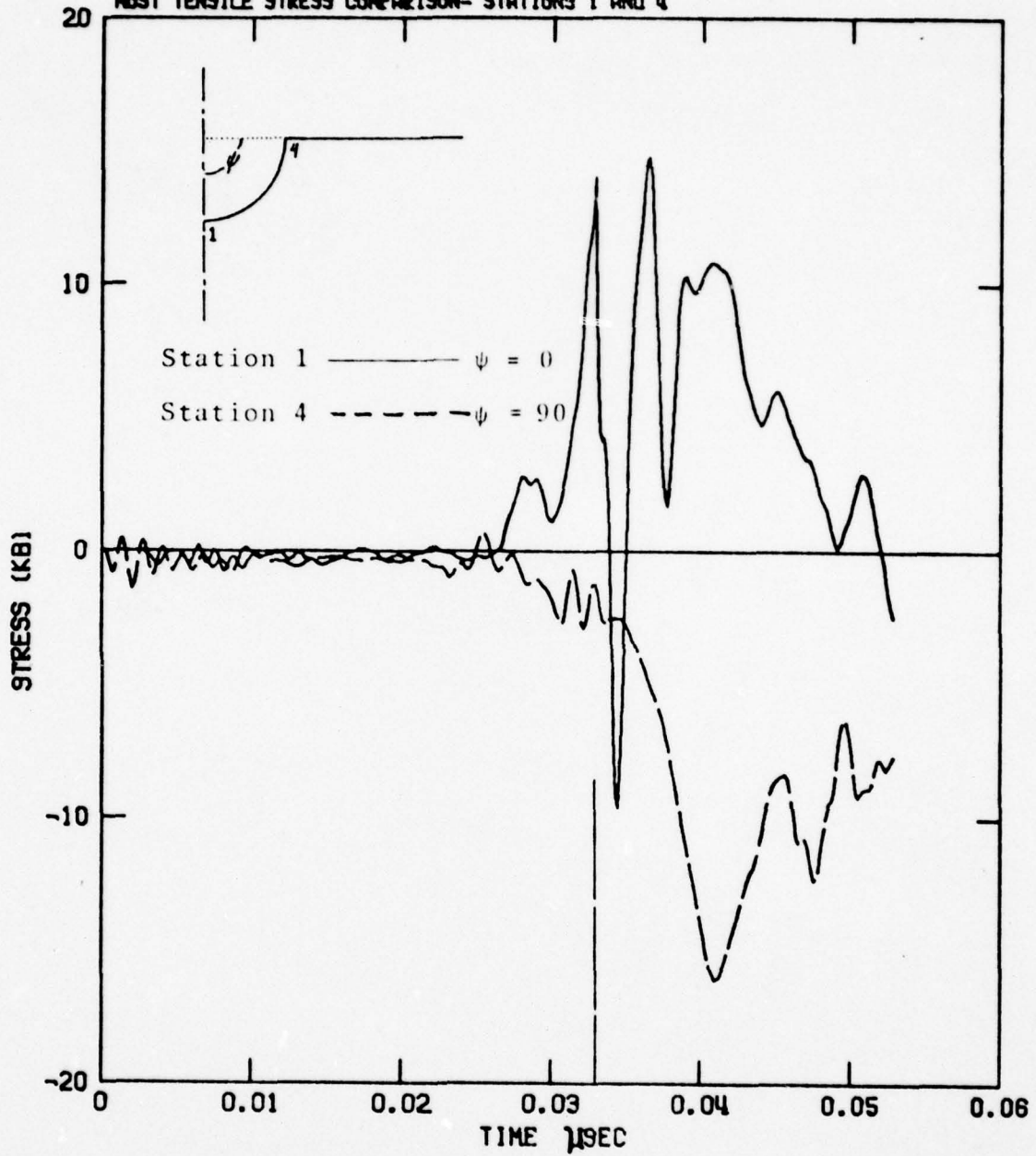
Figure 13. Comparisons of Maximum Principal Tensile Stress versus
Time at Indicated Station (1kb = 100MPa)

21
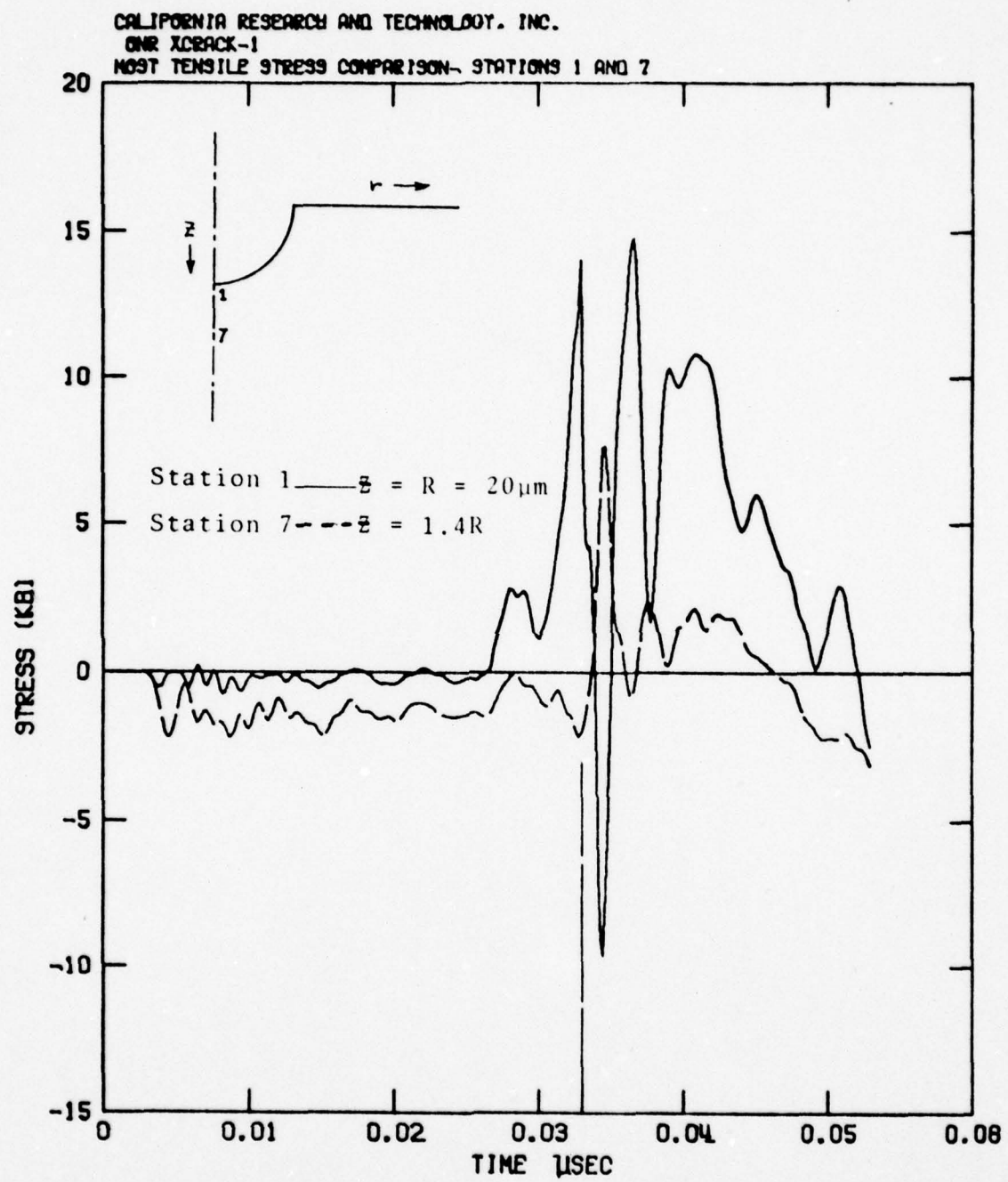
Figure 14. Comparisons of Maximum Principal Tensile Stress versus Time at Indicated Station (1kb = 100MPa)

22
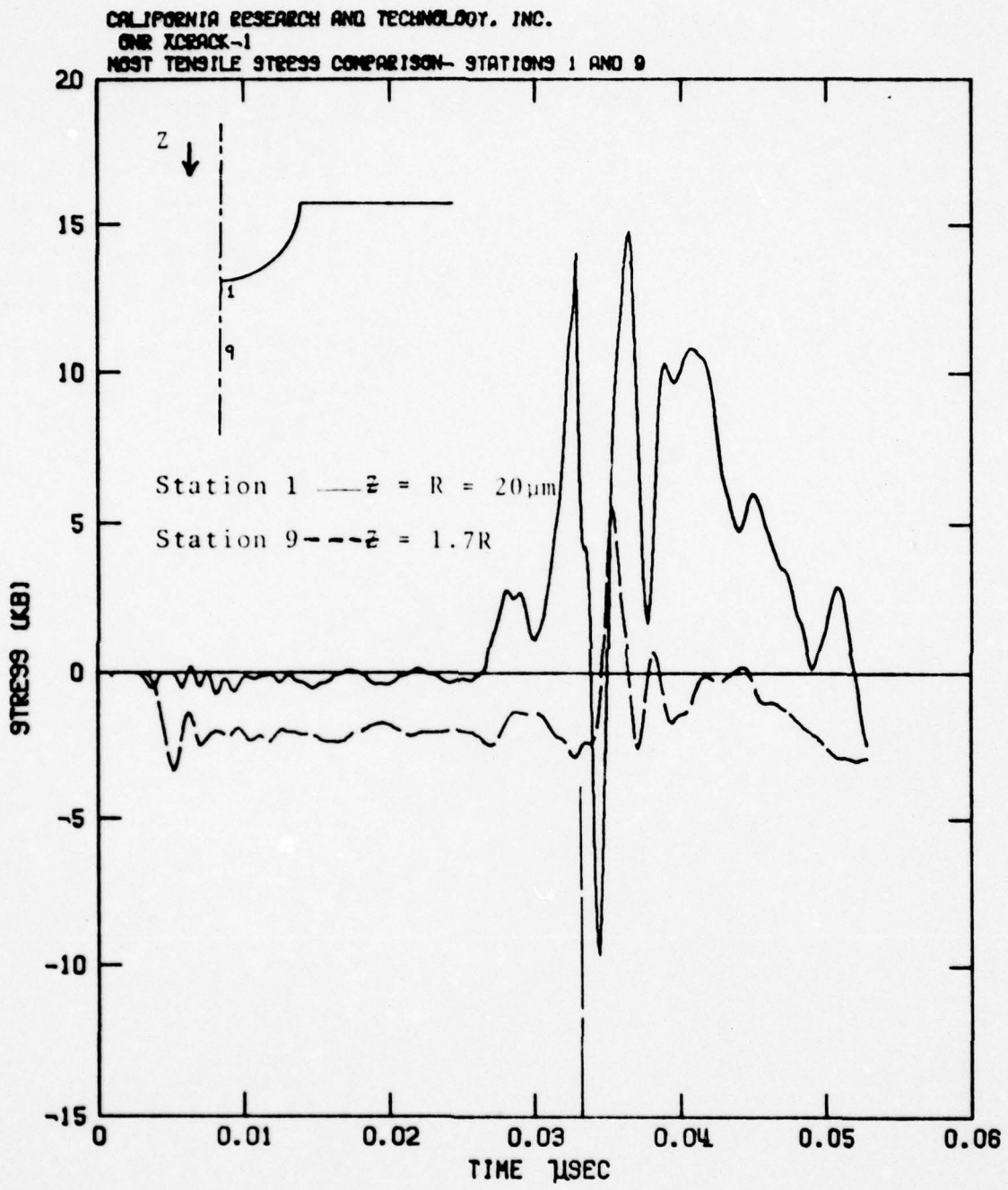
Figure 15. Comparison of Maximum Principal Tensile Stress versus Time at Indicated Station (1kb = 100MPa)

23
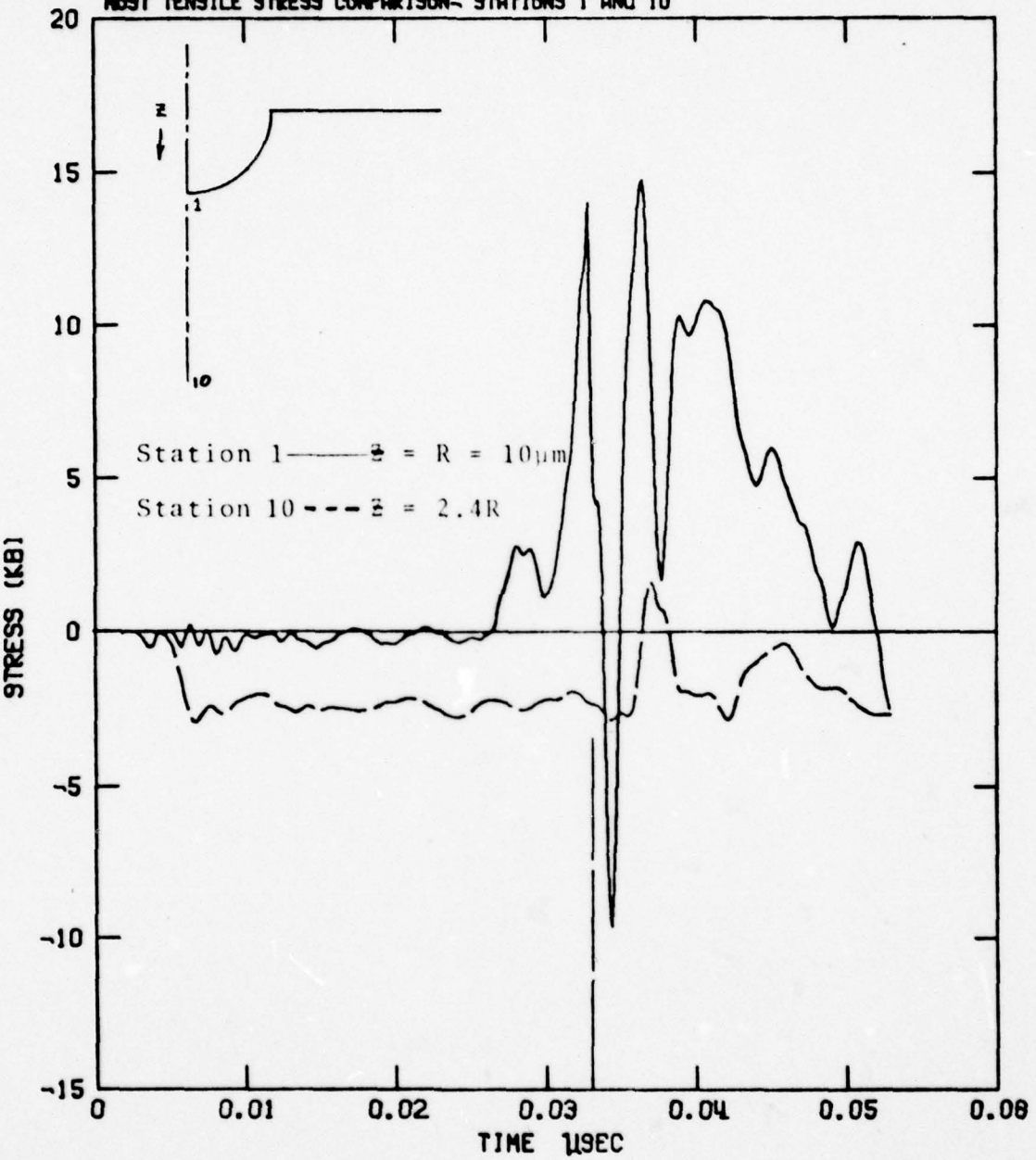
Figure 16. Comparisons of Maximum Principal Tensile Stress versus Time at Indicated Station (1kb = 100MPa)

24
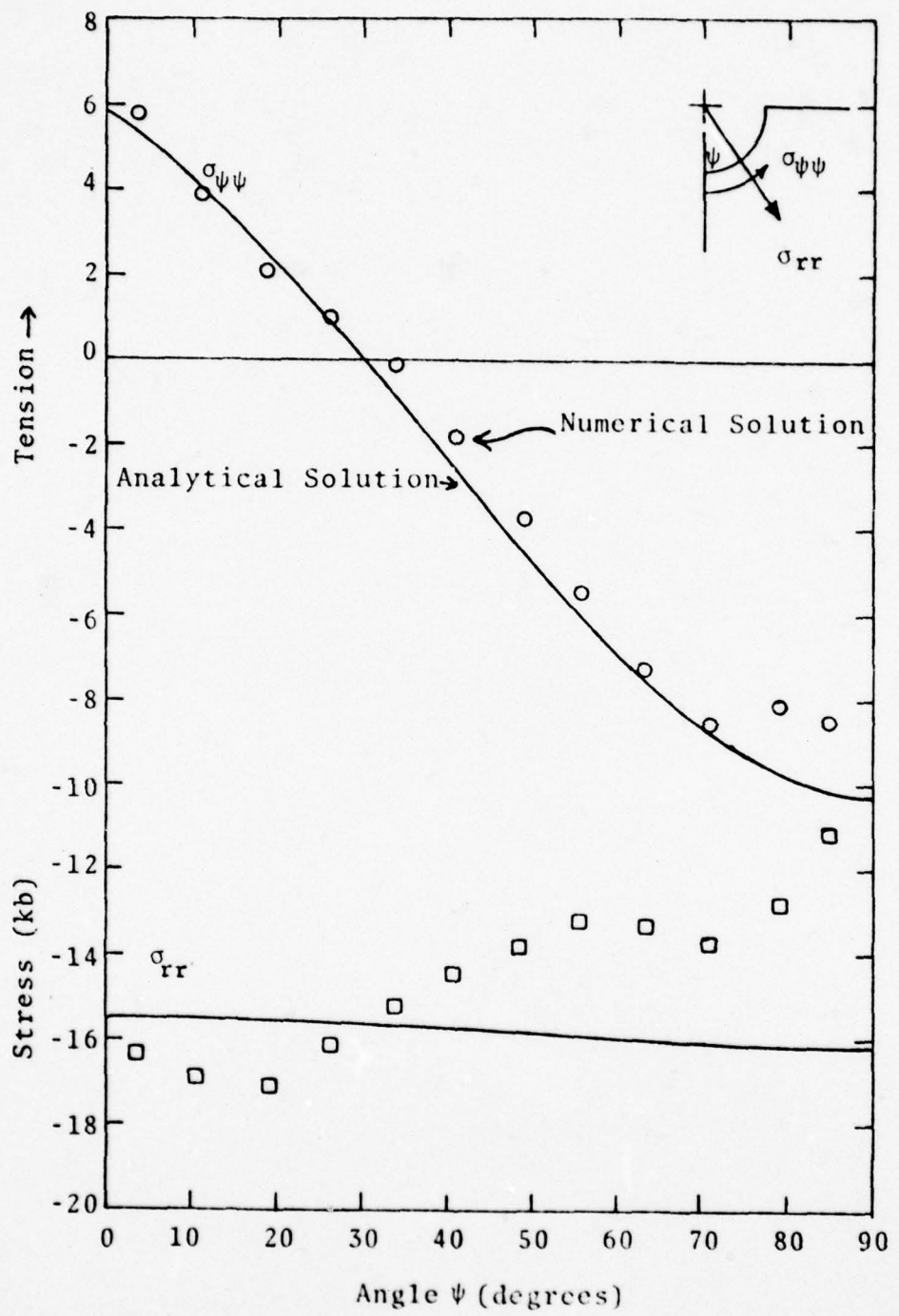
Figure 17. Comparison of Dynamic Numerical Solution with Approximate Static Analytical Solution at 45 Nanoseconds

SECTION III

Strain Energy Release Associated with Circumferential
Cracks around Embedded Particles

STRAIN ENERGY RELEASE ASSOCIATED WITH CIRCUMFERENTIAL CRACKS AROUND EMBEDDED PARTICLES[1]

Y. Marvin Ito, Martin Rosenblatt, Louis Y. Cheng

California Research & Technology, Inc.
Woodland Hills, Ca. 91367

Numerical code simulations are used to determine the strain energy release associated with circumferential cracks around spherical particles embedded in tension within homogeneous matrix materials. It is shown that the fractional release of strain energy $f(\mu)$, where μ is the normalized crack size and $f(0)=1$ for no crack and $f(\pi)=0$ for a crack all around the particle, has a point of inflection at about $\mu=\pi/2$ (hemispherical crack). A *single* point of inflection in $f(\mu)$ confirms the theoretical conditions of crack extension and arrest proposed by Lange [1][2].

Introduction

An *important* area for developing new ceramic materials involves second phase particles embedded within a matrix phase. Due to the usual difference in thermal expansion, highly localized stresses develop as the ceramic is cooled from its fabrication temperature. Thus, these inclusions are usually considered [1] as possible precursors to cracks that form either during cooling or during subsequent stressing. The mechanisms which govern the formation of these cracks are therefore a critical part of the micro-structural behavior of these ceramics.

For the case of a single spherical inclusion of radius R within an infinite medium, a uniform hydrostatic stress $\bar{\sigma}$ develops within the particle and radial and circumferential stresses $\sigma_r = \bar{\sigma} R^3/r^3$ and $\sigma_\theta = -\bar{\sigma} R^3/2r^3$ develop within the surrounding matrix rapidly falling off with increasing distance from the inclusion as shown on Figure 1. The stress $\bar{\sigma}$ due to temperature change ΔT (positive for cooling) is given [2] by

$$\bar{\sigma} = \frac{\Delta\alpha\Delta T}{k} \qquad (1)$$

[2] Figures in brackets indicate the literature references at the end of this paper.
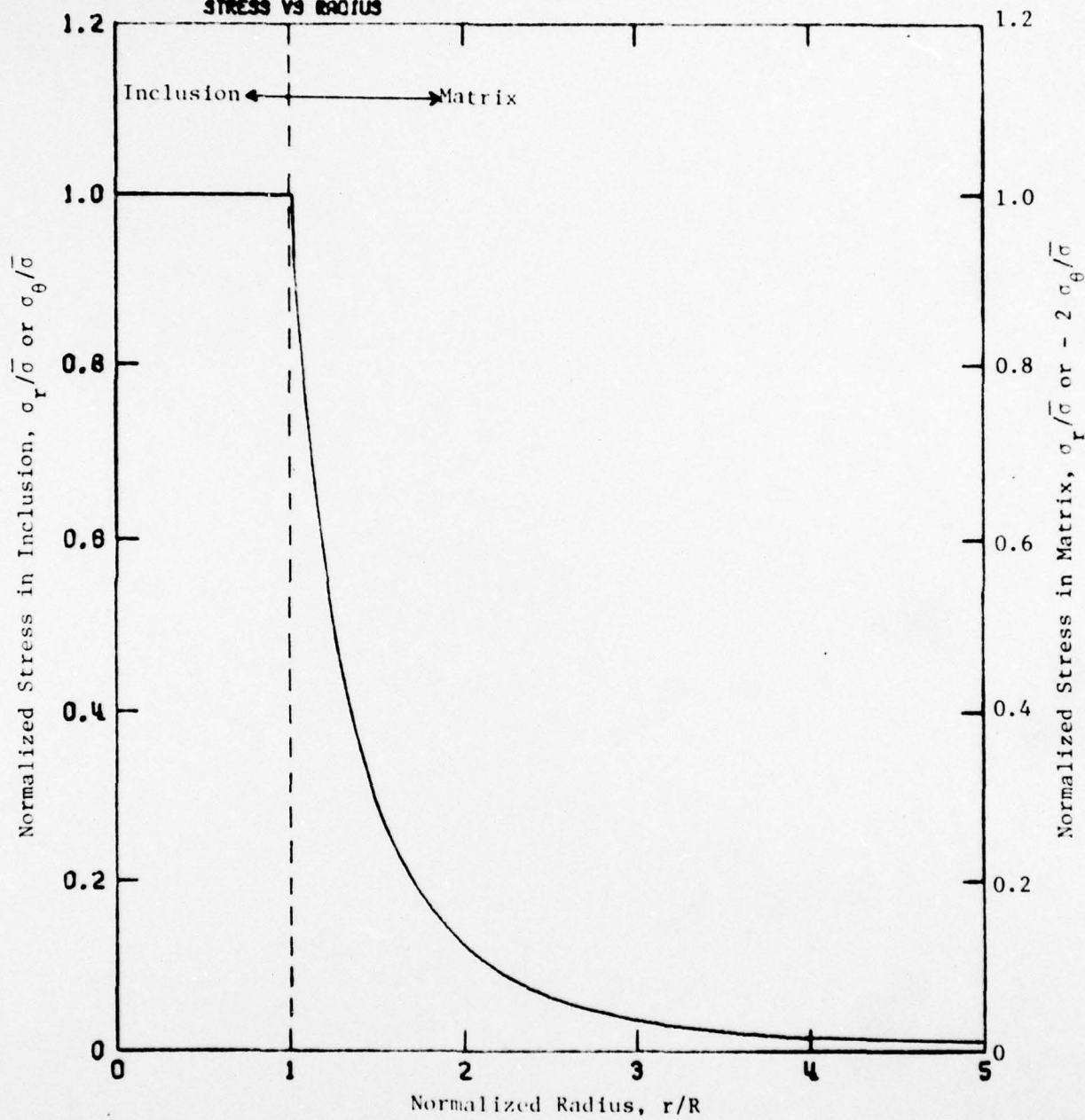
Figure 1. Analytic Solution for Stress Field Near Thermally Strained Spherical Inclusion within Infinite Matrix.

where $k \equiv (1+\nu_m)/2E_m + (1-2\nu_p)/E_p$ and $\Delta\alpha \equiv \alpha_p - \alpha_m$, E is Young's modulus, ν is Poisson's ratio, and α is thermal expansion coefficient. Also, tension is positive and subscripts m and p denote matrix and particle, respectively. (It should be noted that the stress $\bar{\sigma}$ is independent of particle size.) The associated strain energy is [3]

$$U_{SE}^{o} = U_{p}^{o} + U_{m}^{o}$$

$$= 2\pi \frac{\bar{\sigma}^2 (1-2\nu p)}{E_p} R^3$$

$$+ \pi \frac{\bar{\sigma}^2 (1+\nu_m)}{E_m} R^3$$

$$= 2\pi k \bar{\sigma}^2 R^3 \qquad (2)$$

Now consider a crack, which is specified by a single dimensional parameter c, associated with the spherical particle and favorably oriented[3] to the high tensile stress field near the particle/matrix interface. The strain energy associated with the crack/particle/matrix interaction for a given normalized crack size $\mu=c/R$ can be expressed [1] as

$$U_{SE} = U_{SE}^{o} \, f(\mu) \qquad (3)$$

where $f(\mu)$ is a dimensionless function which defines the fractional strain energy release and by definition, $1 \geq f(\mu) \geq 0$.

By hypothesizing that the strain energy release $f(\mu)$ possesses an inflection point, Lange [1] has determined the general criteria for crack extension and arrest in the localized stress fields associated with second phase particles. The unique result of this analysis is that the particle size is one of the key factors that governs the criteria. Thus, for a given material, a critical size exists below which crack extension cannot occur and is given by

$$R_c = \frac{\text{constant}}{\bar{\sigma}^2} \qquad (4)$$

---

[3] For particles in tension ($\Delta\alpha>0$) cracks can occur either within the particle or within the matrix. For particles in compression ($\Delta\alpha<0$) cracks should only occur within the matrix.

This is in direct agreement with experimental observations
[3].

It is the intent of this paper to determine the
explicit function for the release of strain energy associ-
ated with *circumferential* cracks within the highly localized
stress field due to a *spherical* particle embedded *in tension*
within a homogeneous matrix material.

Approach

A circumferential crack associated with a spherical particle
or inclusion placed in tension within a homogeneous material has
the following problem description:

$$\text{Crack}\begin{cases} \text{Angle} \quad \theta = \mu = \dfrac{c}{R} \\[2mm] \text{Area} \quad A = 4\pi R^2(1-\cos\theta) \end{cases}$$
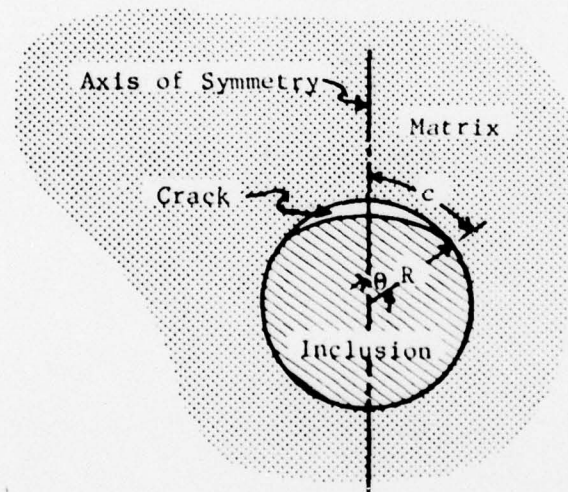
(The inclusion is in hydrostatic
tension and the matrix is in radial
tension and hoop compression.)

A series of *numerical simulations* are performed in order to
examine the quantitative effects of these cracks. The *simulated*
conditions of a single spherical particle of radius R within an
infinite matrix is shown in Figure 2. An inner core region of
radius $a=R/4$ and an outer annulus region of radius $b=3R$ are
simulated by appropriate pressure boundary conditions[4]. A finite-
difference computer code, WAVE-L, with the analytic representation
of the *initial* stress field is used to predict the variation of
the stress field with crack size.

---

[4] The strain energy associated with these regions is less than 5 percent
of the total.
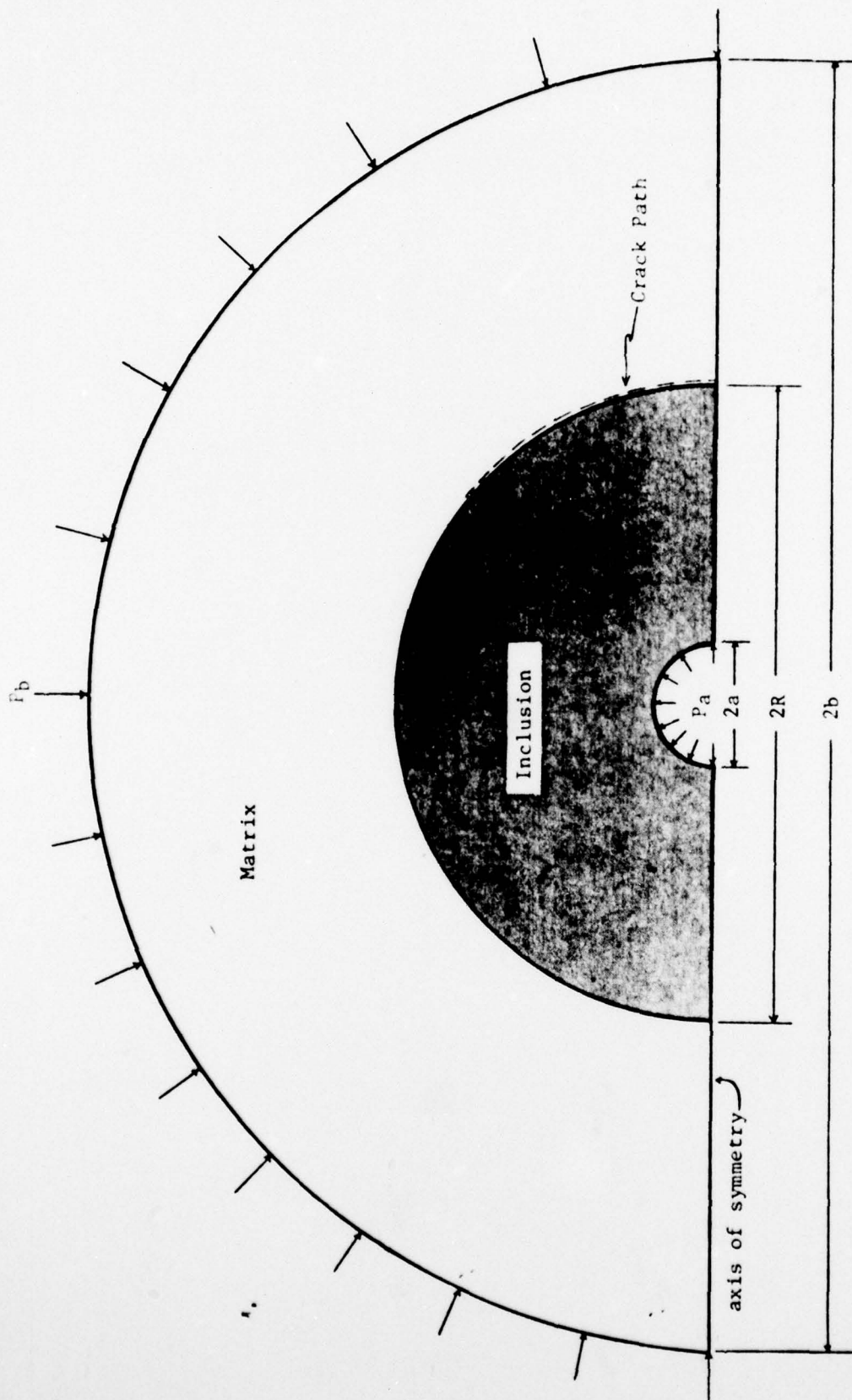
Figure 2. Simulated Conditions of Spherical Inclusion of Radius R Within Infinite Matrix Using Appropriate Pressure Boundary Conditions ($P_a = -\bar{\sigma}$ and $P_b = -\bar{\sigma}/27$ at $a = R/4$ and $b = 3R$, respectively).

WAVE-L is a two-dimensional (axial or plane symmetry), Lagrangian, explicit, finite-difference code based on the HEMP scheme [4] which integrates the governing partial differential equations of motion for arbitrary dynamic or quasi-static problems in solid and fluid mechanics. It has been applied in a number of fracture mechanics investigations, including subsonic water drop impact [5] and quasi-static indentation [6] of ceramics.

The analytic representation of the highly localized stress field (see Fig. 1) is used as the initial conditions for the axisymmetric WAVE-L numerical calculations of the crack/inclusion/matrix interactions. Figure 3 shows the initial computational grid using a cell size of $\Delta r=0.03R$ near the inclusion/matrix interface to resolve the high initial stress gradient to within 10 percent. In the WAVE-L code, velocity (and displacement) is defined at the corners of the computational cells while stress (and strain) state is associated with the center of the cells.

In the numerical code, cracks are simulated as "tensile failure" across computational cells. In a cell with a crack, no tensile stress across the crack is permitted, and no shear stress is permitted on the crack if the crack is open (the width of the crack is continuously monitored). The quasi-static stress (and strain) field is progressively calculated as a crack is incrementally extended along a prescribed path (at the particle/matrix interface in the present investigation).

Strain Energy Release

In the present numerical simulations, the strain energy release is calculated, as a circumferential crack is extended along the particle/matrix interface[5], for embedded particles placed in tension, for three modular ratios. Table 1 gives the material properties and initial conditions for the three cases with modular ratios of $M=1$, $M=1/4$ and $M=4$.

Figure 4 shows the calculated fractional strain energy release function $f(\mu)$. Due to accumulated numerical error as the crack extends, all the strain energy is not released ($f(\pi)\neq0$) as the crack extends all around the particle ($\mu=\pi$). However, the error is no greater than 10 percent for Case 2 ($M=1/4$) and 5 percent for Case 1 ($M=1$) and Case 3 ($M=4$).

Within this numerical accuracy, the present calculations show no significant effect of modular ratio on strain energy release. In all three cases there is a single point of inflection in $f(\mu)$ at about $\mu=\pi/2$. This is shown more clearly on Figure 5 where the derivative $df/d\mu$ has a minimum value at about $\mu=\pi/2$ and compares well with a curve fit with symmetry about $\mu=\pi/2$. Note that $\mu=\pi/2$ corresponds to a hemispherical crack and may be primarily due to geometry effects.

---

[5] The crack is associated with the computational cells in the matrix next to the interface.
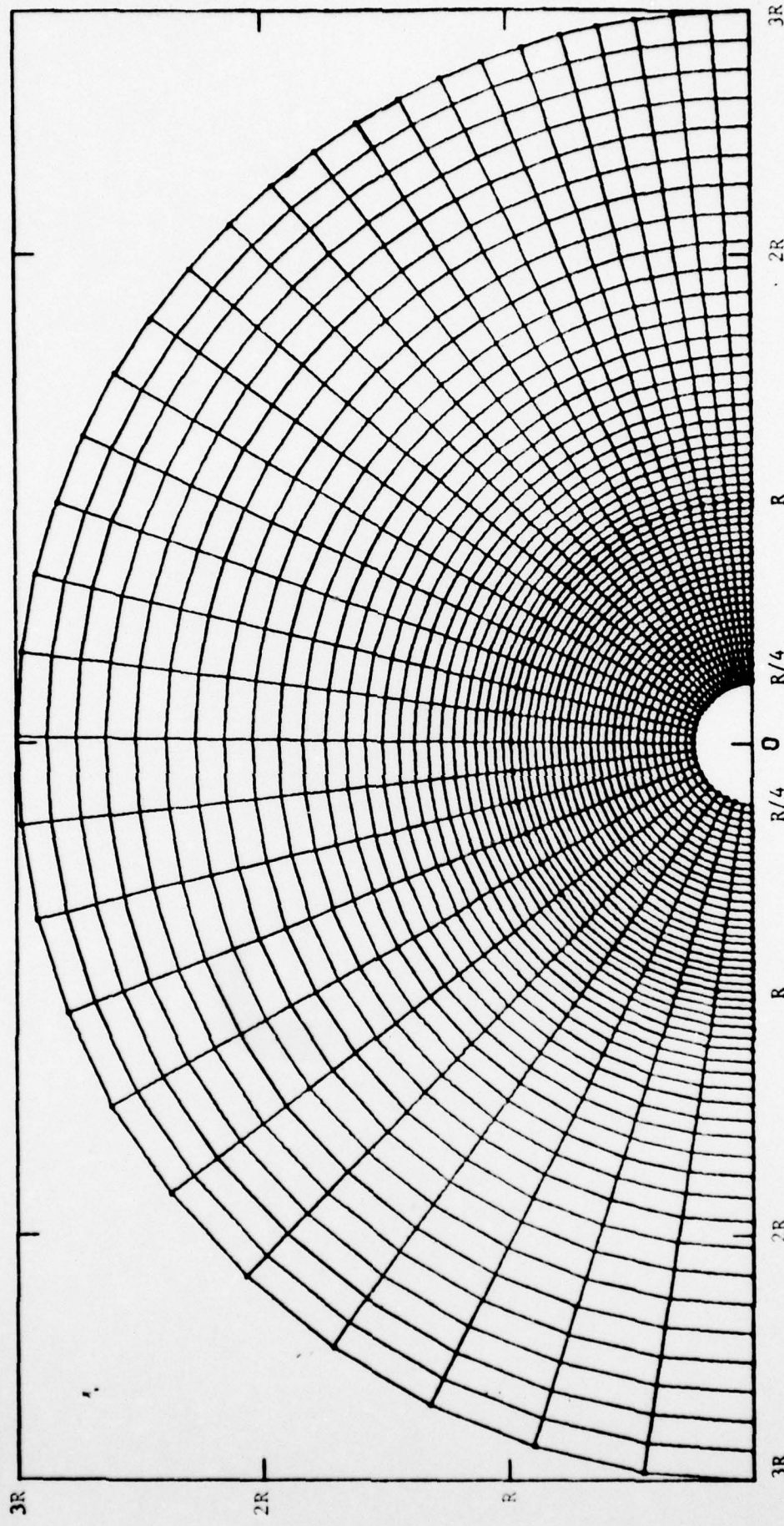
Figure 3. Initial Computational Grid for Simulated Problem of a Spherical Particle of Radius R Embedded Within Infinite Matrix.

TABLE 1. Material Properties and Initial Conditions for Three Modular Ratios.

Case*	Materials	Young's Modulus E(GPa)	Poisson's Ratio ν	Strain Energy Partition $U^o(\mu J)$	Total Strain Energy $U^o_{SE}(\mu J)$	Particle Thermal Contraction $\Delta\alpha\Delta T(\%)$	Particle Hydrostatic Stress $\bar{\sigma}(MPa)$	Modular Ratio $M=E_m/E_p$
1	Alumina Particle	386	0.25	2.87	6.43	0.175	600	1
	Alumina Matrix	386	0.25	3.56				
2**	Alumina Particle	386	0.25	0.36	2.02	0.175	210	0.23
	Glass Matrix	89	0.25	1.66				
3	Glass Particle	89	0.25	2.02	2.60	0.175	240	4.3
	Alumina Matrix	386	0.25	0.58				

* Particle Radius R = 100 μm, Cooling Temperature ΔT = 700°C and Thermal Expansion Coefficient $\Delta\alpha = 2.5 \times 10^{-6}/°C$.

** Outer Boundary at b=2R in this case.
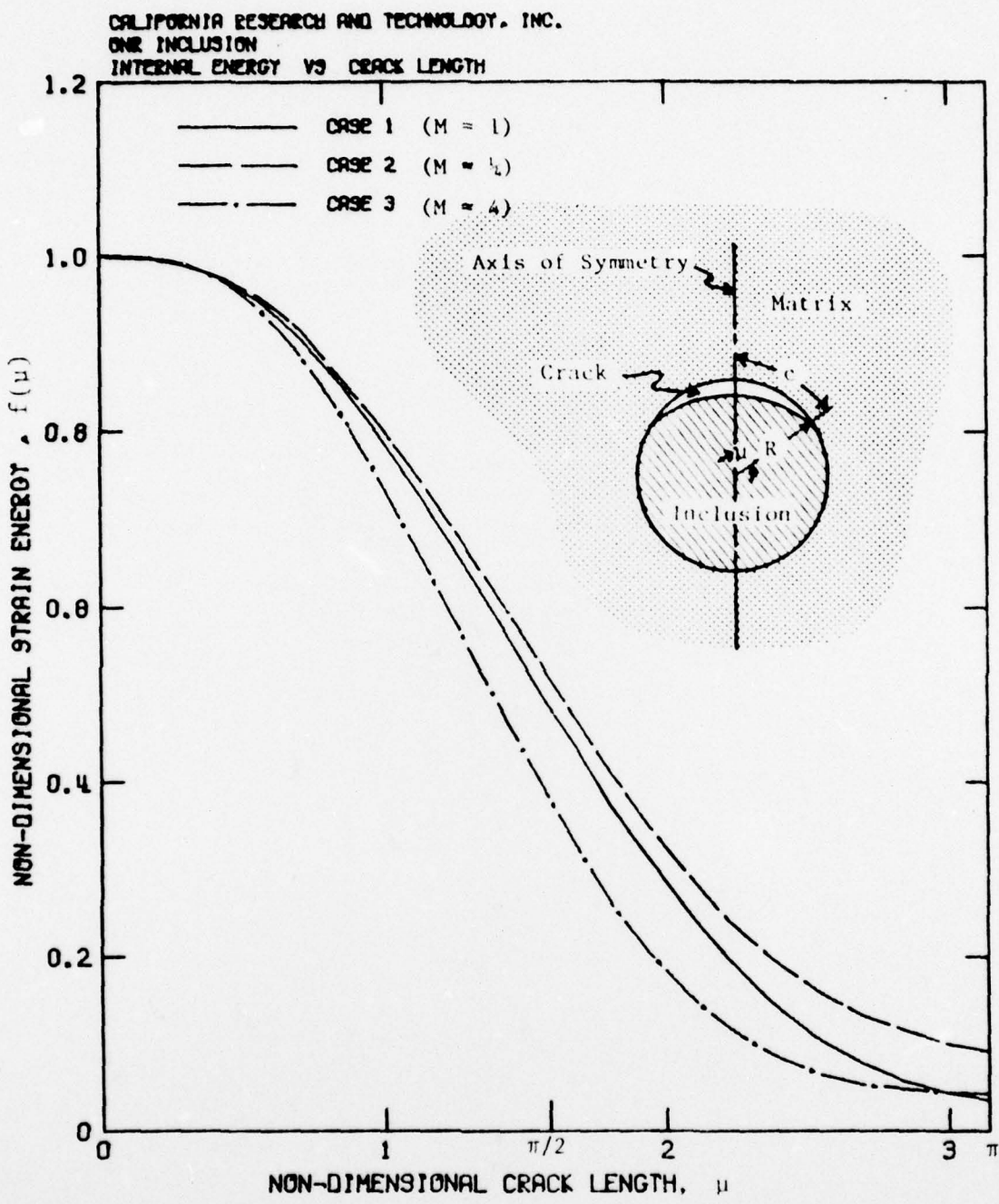
Figure 4. Fractional Strain Energy Release, $f(\mu)$, Versus Normalized
Crack Size, μ, for Three Cases with Modular Ratios of
$M = 1$, $M = \frac{1}{4}$, and $M = 4$.
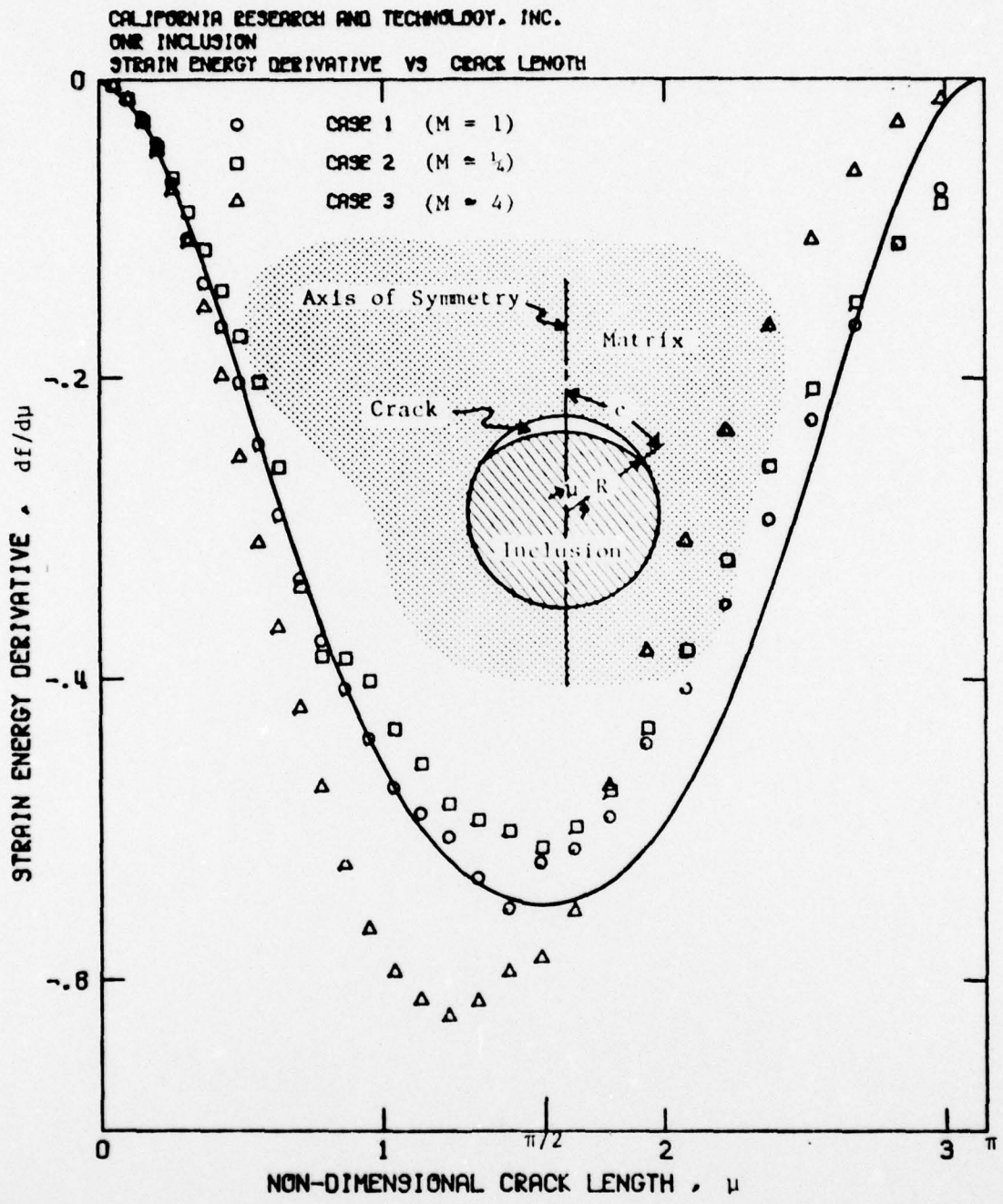
Figure 5. Fractional Strain Energy Derivative, $df/d\mu$, Versus Normalized Crack Size, μ, and Comparison with Analytic Curve Fit.

An analytic curve fit to the calculated results is given in the form

$$f'(\mu) \equiv \frac{df}{d\mu} = -\bar{a}\sin^2\mu + \bar{b}\sin^3\mu \qquad (5)$$

and

$$f(\mu) = -\bar{a}\left(\frac{\mu}{2} - \frac{\sin\mu\,\cos\mu}{2}\right)$$

$$+\bar{b}\left(\frac{\cos^3\mu}{3} - \cos\mu\right) + \bar{c} \qquad (6)$$

Using the conditions $f(0) \equiv 1$, $f(\pi) \equiv 0$ and $f'(\pi/2) = 0.55$ (see Fig. 5), the three constants are

$$\left.\begin{array}{l} \bar{a} = 1.12 \\ \bar{b} = 0.57 \\ \bar{c} = 1.38 \end{array}\right\} \qquad (7)$$

Figures 5 and 6 show this analytic function.

Discussion

The associated strain energy release rate[6] is defined by

$$G \equiv -\frac{dU_{SE}}{dA} \qquad (8)$$

where $A = 4\pi R^2(1-\cos\mu)$ is the surface area of the circumferential crack. It follows from Equations (2), (3) and (5) that

$$G = -U_{SE}^o \frac{f'(\mu)}{4\pi R^2 \sin\mu}$$

$$= -\frac{1}{2}k\bar{\sigma}^2 R \frac{f'(\mu)}{\sin\mu}$$

$$= \frac{1}{2}k\bar{\sigma}^2 R(\bar{a}\sin\mu - \bar{b}\sin^2\mu) \qquad (9)$$

Hence, from Lange [1], using the thermodynamic criterion introduced by Griffith [7], crack extension will occur when the value of G for a given crack size is equal to γ and crack arrest occurs at a value of μ where $G \leq \gamma$, where γ is the fracture energy. This is shown in Figure 7 using Case 1 properties (see Table 1) and a nominal value of $\gamma = 10$ J/m². Regardless of the crack size, crack

---

[6] The stress intensity factor can be derived through $K = \sqrt{GE}$.
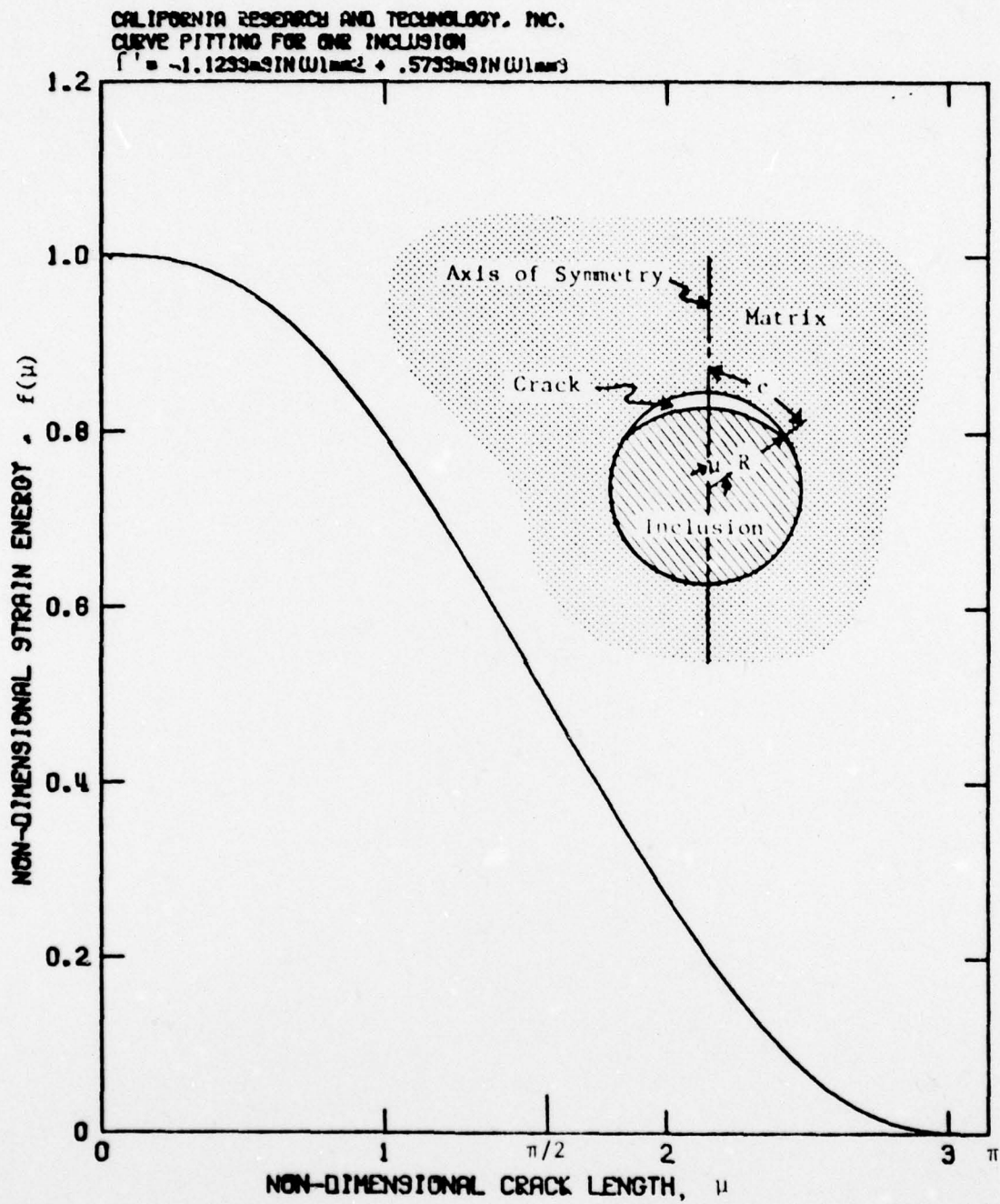
Figure 6. Analytic Representation of Fractional Strain Energy Release,
f(μ), Versus Normalized Crack Size, μ.

Figure 7. Strain Energy Release Rate for Crack Extension and Arrest
Using Case 1 Properties from Table 1.

extension can only occur when the G versus μ function exceeds γ which first occurs, in the present analysis, when

$$\overline{\sigma}^2 R \geq \frac{2\gamma}{k(\overline{a}-\overline{b})} \qquad (10)$$

Also, Equation (4) becomes

$$R_c = \frac{2\gamma}{k\overline{\sigma}^2(\overline{a}-\overline{b})} \qquad (11)$$

The present investigation obtained G for the case of circumferential cracks associated with isolated embedded particles placed in tension. Radial cracks [1] are observed for embedded particles placed in compression, and thus would require a separate solution for G. Also, future solutions would involve particle-to-particle interactions for the case where the inter-particle separation is less than one particle diameter.

References

[1] Lange, F. F., Criteria for Crack Extension and Arrest in Residual, Localized Stress Fields Associated with Second Phase Particles, Fracture Mechanics of Ceramics, Vol. 2, ed. by Bradt, Hasselman and Lange, pp. 599-613 (Plenum Press, New York, 1974).

[2] Selsing, J., Internal Stresses in Ceramics, J. Am. Ceram. Soc. 44, 419 (1961).

[3] Davidge, R. W. and Green, T. J., The Strength of Two-Phase Ceramic/Glass Materials, J. Mat. Sci. 3, 629 (1968).

[4] Wilkins, M. L., Calculation of Elastic-Plastic Flow, Report UCRL-7322, Rev. I, Lawrence Radiation Laboratory, University of California, Livermore, California (1969).

[5] Ito, Y. M., Rosenblatt, M., Perry, F. W., and Eggum, G. E., Analysis of Water Drop Erosion Mechanisms in Infrared-Transparent Materials using Microphysical Fracture Models, Report AFML-TR-77-219, Air Force Materials Laboratory, Wright-Patterson Air Force Base, Ohio (1977).

[6] Rosenblatt, M. and Eggum, G. E., Unpublished work at California Research and Technology (1976).

[7] Griffith, A. A., The Phenomena of Rupture and Flow in Solids, Phil. Trans. Roy. Soc. London. 221A, 163 (1920).